UNIVERSITY OF CALIFORNIA SAN DIEGO

Physically Assisted Signal Processing in High-Capacity Systems

A dissertation submitted in partial satisfaction of the

requirements for the degree Doctor of Philosophy

in

Electrical Engineering (Photonics)

by

Zahra Serahati Jouybari

Committee in charge:

Stojan Radic, Chair
Nikola Alic
Leonid Butov
Miroslav Krstic
Zhaowei Liu
George C. Papen

2021

The Dissertation of Zahra Serahati Jouybari is approved, and it is acceptable in quality and form for publication on microfilm and electronically.

University of California San Diego

2021

DEDICATION

To my family and friends

For their love and support

TABLE OF CONTENTS

LIST OF FIGURES

LIST OF ABBREVIATIONS

AI	Artificial Intelligence
1G	First Generation Mobile Network
5G	Fifth Generation Mobile Network
M2M	Machine-to-Machine
IoT	Internet of Things
MMW	Millimeter-Wave
BW	Bandwidth
RF	Radio Frequency
GbE	Gigabit Ethernet
TbE	Terabit Ethernet
CD	Chromatic Dispersion
ISI	Intersymbol Interference
VNA	Vector Network Analyzer
NLSE	Nonlinear Schrödinger Equation
SOP	State of Polarization
MZM	Mach-Zehnder Modulator
IMDD	Intensity Modulation and Direct Detection
CW	Continuous-Wave

LO	Local Oscillator
RIN	Relative Intensity Noise
ASE	Amplified Spontaneous Emission
PC	Polarization Controller
QAM	Quadrature Amplitude Modulation
BER	Bit-Error Rate
QF	Quality Factor
AWGN	Additive White Gaussian Noise
DSP	Digital Signal Processing
PDM	Polarization Division Multiplexing
DAC	Digital-to-Analog Converters
PBS	Polarization Beam Splitter
PBC	Polarization Beam Combiner
EDFA	Erbium-Doped Fiber Amplifier
TIA	Trans-Impedance Amplifier
ADC	Analog-to-Digital Converter
PMD	Polarization Mode Dispersion
XPM	Cross-Phase Modulation

FWM	Four-Wave Mixing
OPLL	Optical Phase-Locked Loop
CPE	Carrier Phase Estimation
SMF	Single-Mode Fiber
GBd	Gigabaud
FIR	Finite Impulse Response
YIG	Yttrium Iron Garnet
MEMS	Microelectromechanical Systems
CFBG	Chirped Fiber Bragg Gratings
BOS	Broadband Optical Sources
EO	Electro-Optic
TOD	Third Order Dispersion
DCF	dispersion compensating fiber
VDL	Variable Delay Line
OSNR	Optical Signal-to-Noise Ratio
AWG	Arbitrary Waveform Generator
IP	Internet Protocol
ENOB	Effective Number of Bits

ASICs	Application-Specific Integrated Circuits
CMOS	Complementary metal-oxide-semiconductor
FDSOI	Fully Depleted Silicon on Insulator
HBT	Heterojunction Bipolar Transistor
BiCMOS	Bipolar CMOS
MI	Modulation Instability
HNLF	Highly Nonlinear Fiber
DF-HNLF	Dispersion-Flattened HNLF
FoM	Figure of Merit
NF	Noise Figure
EO	electro-optic
OE	opto-electronic
ETDM	electronic time-division multiplexing
DBI	digital bandwidth interleaving

ACKNOWLEDGEMENTS

First, I would like to express my sincere gratitude to my advisor, Professor Stojan Radic. With his guidance and support, I am where I am today. To me, Photonic system lab has not only been a research lab, but a safe home and I love every inch of it. Besides, I would like to thank all my committee members: Professor Butov, Professor Krstic, Profosser Liu, Professor Papen and Doctor Nikola Alic for their constructive discussions and contributions into this dissertation.

I would like to express my deep gratitude to my co-advisor, Dr. Nikola Alic. In this PhD journey, he has always been by my side. I cannot say enough, in the pandemic, how much I missed our morning ritual; him standing by my desk with his cup of coffee in his hand, smiling and asking me if I see the light at the end of the tunnel. Besides sharing his valuable knowledge with me, he taught me how to break down the problem into smaller pieces, be patient and solve it step by step. This is one of the most precious takeaways for me and I am forever grateful for that.

I would like to thank my first mentor, Dr. Vahid Ataie, for generously sharing his valuable knowledge with me. While introducing me to the basics of the experiments in the lab and making this transition easier, he reminded me of the importance of independent research.

Many thanks to Dr. Evgeny Myslivets and Dr. Eduardo Temprana who have helped me in the RF-Photonic filter implementation. Their passion for what they are doing has always motivated me to be more committed and focused on my project. I would like to also thank Dr. Bill Kuo who has never hesitated to help me with his valuable advice.

A special thank to our lab members, Dr. Huan Hu, Dr. Jin Zhang, Motohiko Eto, Jasen Leng, Dr. Ana Pejkic, and Dr. Liangshun Han for their help and support during my PhD and

brightening my daily life. The pandemic made me truly realize how much I appreciate their company.

Chapter 3, in part, is a reprint of the material as it appears in Journal of Lightwave Technology, vol. 38, no. 6, pp. 1194–1201, (2020), titled “Demonstration of a Sub-GHz Flat-Top Comb-Based RF-Photonic Filter Enabled by Fourth-Order Dispersion Compensation” by Zahra Serahati, Eduardo Temprana, Evgeny Myslivets, Vahid Ataie, Nikola Alic, and Stojan Radic. In addition, Chapter 3, in part, is a reprint of the material as it appears in 2019 IEEE Photonics Conference (IPC), 2019, pp. 1–2, titled “Demonstration of the First Sub-GHz Comb-based RF-Photonic Flat-top Filter” by Zahra Serahati, Eduardo Temprana, Evgeny Myslivets, Vahid Ataie, Nikola Alic, and Stojan Radic. Lastely, Chapter 3, in part, is a reprint of the material as it appears in Frontiers in Optics 2019, paper FTu5B.5., titled “Compensation of Fourth-Order Dispersion Induced Distortion in Comb-Based Microwave Photonic Filters” by Zahra Serahati, Eduardo Temprana, Evgeny Myslivets, Vahid Ataie, Nikola Alic, and Stojan Radic. The dissertation author was the primary investigator and the primary author of these articles.

Chapter 4, in part, is a reprint of the material submitted to IEEE Photonics Journal, titled “Parametric Channelizer Assisted Chromatic Dispersion Compensation in High-Baud Rate Coherent Systems” by Zahra Serahati, Nikola Alic, and Stojan Radic. The dissertation author was the primary investigator and the primary author of this article..

VITA

2012 Bachelor of Science, Electrical Engineering (Telecommunications), K.N.Toosi University of Technology, Iran

2015 Master of Science, Electrical Engineering (Fields and Waves), University of Tehran, Iran

2021 Doctor of Philosophy, Electrical Engineering (Photonics), University of California San Diego, USA

PUBLICATIONS

Journal articles:

Zahra Serahati, Eduardo Temprana, Evgeny Myslivets, Vahid Ataie, Nikola Alic, and Stojan Radic, "Demonstration of a Sub-GHz flat-top Comb-based RF-Photonic Filter Enabled by Fourth-order Dispersion Compensation", Journal of Lightwave Technology, vol. 38, no. 6, pp. 1194–1201, 2020.

Zahra Serahati, Nikola Alic, and Stojan Radic, "Parametric Channelizer Assisted Chromatic Dispersion Compensation in High-Baud Rate Coherent Systems", submitted to IEEE Photonics Journal.

Conference proceedings:

Zahra Serahati, Eduardo Temprana, Evgeny Myslivets, Vahid Ataie, Nikola Alic, and Stojan Radic, "Demonstration of the First Sub-GHz Comb-based RF-Photonic Flat-top Filter," In IEEE Photonics Conference (IPC), pp. 1-2, 2019.

Zahra Serahati, Eduardo Temprana, Evgeny Myslivets, Vahid Ataie, Nikola Alic, and Stojan Radic, "Compensation of Fourth-Order Dispersion Induced Distortion in Microwave Photonic Filters using Pulse Shaper" In Frontiers in Optics, paper FTu5B.5, Optical Society of America, 2019.

ABSTRACT OF THE DISSERTATION

Physically Assisted Signal Processing in High-Capacity Systems

by

Zahra Serahati Jouybari

Doctor of Philosophy in Electrical Engineering (Photonics)

University of California San Diego, 2021

Professor Stojan Radic, Chair

Although it may seem mundane, we have been and we continue to face an extensive and seemingly never ending growth trend of data traffic: in terms of the increase in the number of network users, as well as the emergence of new bandwidth-hungry applications and services, and certainly driven by the unprecedented cloud computing, high-definition videos, Artificial Intelligence, and the Internet of Things. The former predicament implies that the backbone of our fixed broadband, wireless, and optical communication networks needs to be well-equipped to facilitate this evolution and accommodate the need for higher capacity systems. Specifically, the

new generation 5G network's frequency spectrum extends from several MHz to the Milimeter-wave region and supports a wide variety of signal bandwidths and carrier spacings. Through this flexible framework, the recently launched wireless network serves various users and applications. On the other hand, the coherent optical communication network is also experiencing a shift toward higher bandwidth optical signals with qaudrature amplitude modulation. The transmission of 220GBd QPSK [1] and 128GBd 16-QAM [2] optical signals have already been demonstrated and the baud rate of QAM modulation formats has increased with a pace of 12 GBd per year over the last decade[3].

The aim of this dissertion work was to investigate the utilization of hybrid optoelectronic subsystems in high capacity communication networks which may offer functionalities which are difficult, or even impossible to achieve with the existing all-electronic subsystems. In this dissertation, the hybrid optolectronic subsystems for either wireless network, or coherent optical communication network were proposed. Specifically, in these subsystems, optical and electrical components with bandwidths compatible with commercially available devices are utilized. Thus, they pave the way to the realization of more robust, cost-effective, and higher capacity communication systems. In this respect, the first experimental demonstration of a sub-GHz flat-top comb-based RF-photonic filter is reported in this dissertation. The high quality flat-top spectral shape and shape-invariant tuning of the filter center frequency was enabled by a precise higher order dispersion compensation, for the first time. Furthermore, successful retrieval of digitally modulated RF signals at different center frequencies with varying symbol rates for QPSK and 16-QAM modulation additionally verified the filter integrity. The extended experimentation clearly demonstrated that this new narrowband flat-top filter can be used as a simultaneously tunable and

programmable filter at remote 5G nodes, which correspondingly relaxes the need for high-resolution ADCs.

Furthermore, within the realm of fiber optic transport, we have proposed and investigated channelizer-assisted chromatic dispersion compensation in high baud rate coherent systems. Chromatic dispersion penalty is a crucial signal impairment which scales as a square of the (symbol) signal rate and will severely limit the transmission reach if not mitigated efficiently. Our findings have shown that transmission reach can be more than tripled when resorting to this physically-aided processing strategy, as opposed to the standard digital processing – only approach.

Chapter 1 Introduction

1.1.Motivation

As we witness an ever-increasing trend of internet usage in our daily lives, including mobile (cellular) connections, high-definition videos, online games, social media, cloud computing, healthcare monitoring, autonomous vehicles, and cloud-based Artificial Intelligence (AI), it is foreseeable that the global internet capacity will increase immensely – perhaps incomprehensably in the coming years. Considering the history of mobile communication networks, reviewed in Figure 1. 1, we can clearly notice a significant leap in capacity occurring every 10 years. Starting with the voice-only communication in the First Generation (1G) mobile network in the 1980s, today's Fifth Generation (5G) mobile network is a common platform for various applications. It supports person-to-machine, machine-to-machine (M2M), as well as person-to-person connection. In fact, the Internet of Things (IoT) has become a widespread system wherein people, data, processes, and physical objects connect to the internet and each other [4].

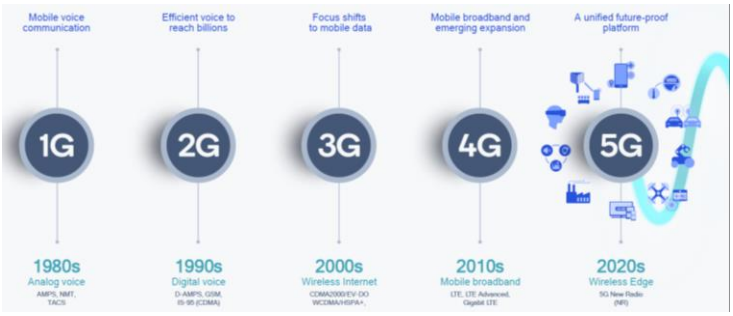

Figure 1. 1 The evolution of mobile communication networks [5].

As reported in CISCO Annual Internet Report released in 2020 [4], and shown in Figure 1. 2, the total number of global mobile subscribers will increase from 5.1 billion (66 percent of population) in 2018 to 5.7 billion (71 percent of population) by 2023. It is also predicted that we

will observe an increase in the number of mobile devices from 8.8 billion in 2018 to 13.1 billion by 2023, wherein 4.1 billion of those will be 5G capable. Among mobile devices, the fastest-growing category is M2M followed by smartphones. Moreover, the fixed broadband and cellular speeds will more than double and triple, respectively, by 2023. The speed increase itself promises the overall use increase [4].

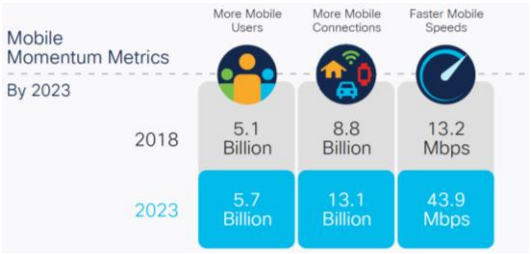

Figure 1. 2 Global mobile networking metrics [4].

The 5G network operates on a wide range of frequencies, from several MHz to the 100 GHz, the Millimeter-Wave (MMW) range. The 5G entails a widely scalable numerology, i.e., the choice of different subcarrier spacing, symbol duration, and the number of symbols per time slot [6]. And through this flexible framework, it can address diverse users and services. In 5G, depending on the frequency range of operation, as shown in Figure 1. 3, different system bandwidths (BWs) are defined [7]. The low end of the bandwidth scale can be utilized for massive machine connectivity. On the other hand, very wide BWs may be dedicated to high-capacity scenarios, e.g., 4K videos [8] and beyond.

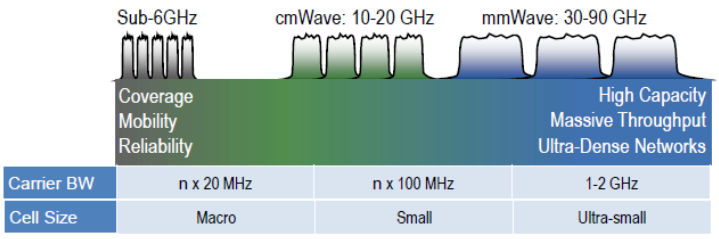

Figure 1. 3 Carrier bandwidth in different parts of the frequency spectrum covered in 5G [9].

Furthermore, the rapid increase of internet usage has urged both research and industry communities to explore ways to increase the capacity and the efficiency of bandwidth utilization in optical communication systems. In coherent optical fiber communication systems, particularly, different multiplexing and modulation schemes have been studied to expand the total system capacity [3]. In single-carrier coherent optical transmission, a growing trend in the symbol rate or the bandwidth of the signal has been observed over the last decade [3].

Consequently, the electrical and optical infrastructure of our communication networks should accommodate the required changes to support a high-capacity, reliable, and cost-effective data transmission. Electronic subsystems, e.g., Radio Frequency (RF) filters, might be needed in a wireless base-station that support various signal bandwidth in different frequency ranges covered by 5G. The agile tunability and programmability could be the critical features of these subsystems. Or, in high-speed coherent transmission systems, we need optical transceivers that support the high-bandwidth optical signals. Moreover, at higher bandwidths, the digital mitigation of the transmission impairment and signal distortion becomes critical, which indicates the importance of high-speed and high-resolution digitizers and digital signal processors. While the 400 Gigabit Ethernet (GbE) has already been established in our commercial optical systems and deployment of 800GbE or even 1.6 Terabit Ethernet (TbE) in the coming years is anticipated [3], the commercially available electronics cannot keep up with the increase of the optical data rates [10]–[12].

On the other hand, photonic technologies offer spectacular features. The low cost and almost vanishingly small propagation loss, the immunity to electromagnetic interference, and the huge processing bandwidth of the optical fibers make them more than an adequate platform for signal processing [13], [14]. Additionally, the optical frequency combs and parametric wavelength

multicasting has been a useful tool in optical signal processing [15]. Hybrid optoelectronic subsystems could be designed using the existing commercially available electronic and optical components with the same functionalities as their all-electronic counterparts, which often offer equivalent or even better performance.

Our goal, in this dissertation, was to utilize these outstanding features of photonics to design or implement hybrid optoelectronic subsystems which may prove critical for the realization of higher capacity communication systems.

1.2.Dissertation Overview

This dissertation consists of treatise of analog photonic wireless (i.e. an RF-photonic filter with possible application in 5G wireless base stations) as well as digital application realms. In the former, the design and implementation of the first sub-GHz flat-top RF-photonic filter is demonstrated. The programmability and shape-invariant frequency tunability of this filter promise its application in the high capacity 5G network covering a broad spectrum. On the other hand, within the area of digital fiber optic communications, in a spectrally sliced optical coherent receiver, the sub-channel digital chromatic dispersion (CD) mitigation of the high baud rate signals has been investigated employing a parametric optical channelizer.

Our main tool for optical signal processing in the aforementioned subsystems was the parametric optical frequency comb, whose optical emission spectrum consists of a series of equally spaced (frequency) mutually coherent lines. These frequency combs have been studied extensively, both theoretically and experimentally, in our research group [16]–[18].

One of the important effects in optical fibers (and waveguides as a whole), which has exhibited a bittersweet characteristic in this dissertation, is chromatic dispersion. On the positive side, chromatic dispersion helped us introduce a frequency-dependent time delay in the implementation of the RF-photonic filter, albeit, a precise control of the dispersion was required to achieve this goal. On the other hand, in optical communication, chromatic dispersion in the fiber links causes time-domain interference between transmitted symbols and consequently momentous errors and penalties in the data retrieval at the receiver. In our designed spectrally sliced high baud rate coherent receiver, we have digitally mitigated the CD penalty in each detected sub-channel and successfully retrieved the transmitted data. In particular, the research presentation in the thesis has been divided as follows:

Chapter 2 serves as a review of the relevant background regarding propagation in optical fibers and the equations describing the pulse propagation and the chromatic dispersion effect. Coherent detection and the optical signal quality metrics in coherent transmission systems are discussed. After a brief review of the configuration of a digital coherent optical transmission system, the digital signal processing chain in coherent transmitter and receiver is discussed.

In chapter 3, the implementation of the first sub-GHz flat-top RF-photonic filter based on phase and amplitude control of a parametric optical frequency comb is demonstrated. First, the transfer function of the filter is characterized using a Vector Network Analyzer (VNA). The designed filter response and shape-invariant tuning of the filter center frequency are achieved by precise third and fourth-order dispersion compensation using a pulse shaper. The filter implentation was the first demonstration of the fourth-order dispersion compensation in these RF-photonic filters and its theoretical investigation is also provided in chapter 3. Moreover, a rigurous

characterization of the filter integrity by the retrieval of a set of digital modulated RF channels had also been performed and is presented.

Chapter 4 proposes a new spectrally sliced coherent receiver configuration for the detection of high baud-rate optical signals using a parametric optical channelizer. The principle of parametric optical channelizer, digital mitigation of CD in each sub-channel, and signal reconstruction using a digital filter bank is explained. Following that, we present the numerical simulation results for CD compensation in 214GBd QPSK and 107GBd 16-QAM signal transmission using, respectively, an 8- and 4-channel parametric optical channelizer. Moreover, an improved performance of the parametric channelizer-assisted CD compensation over full-bandwidth detection is represented. It is demonstrated that parametric channelizer-assisted CD compensation, empowered by reliance on high-resolution low-speed digitizers, significantly extends the transmission reach for high baud rate coherent optical signals.

Lastly, Chapter 5 summarizes this dissertation and discusses the future work.

Chapter 2 Background

2.1.Introduction

The role of the optical fiber in this dissertation was that of providing a platform for processing the data in the optical domain as well as serving as a waveguiding medium and enabling propagation of the information-bearing signals in optical communication systems. In this chapter, first, we review the pulse propagation in fiber and the corresponding governing equations. Then, chromatic dispersion, which, as previously emphasized played an exceedingly important role in this dissertation will be explained. The basics of the coherent optical communication, transmission systems, and digital signal processing in these systems, e.g., a digital filter for chromatic dispersion compensation will be introduced and discussed. It is also worth mentioning that the material reviewed in this chapter serves as a background for the finite impulse response (FIR) RF-photonic filter discussed in chapter 3, as well as for the optical channelizer-assisted CD compensation in high baud rate coherent receivers discussed in chapter 4.

2.2.Pulse Propagation in Optical Fiber

Assuming that the optical field is quasi-monochromatic, i.e., its spectral width $\Delta\omega$ is very small relative to the spectrum center frequency ω_0 ($\frac{\Delta\omega}{\omega_0} << 1$), the pulse propagation in fiber is governed by Nonlinear Schrödinger Equation (NLSE) [19]. This is a valid assumption for pulse width$\gtrsim$0.1ps ($\Delta\omega \lesssim 10^{13}s^{-1}$) since the spectrum is usually centered around 1.55nm ($\omega_0 \sim 10^{15}s^{-1}$) in optical communication and applications of interest in this dissertation. The governing equation is

$$\frac{\partial A}{\partial z}+\frac{\alpha}{2}A-j\sum\nolimits_{n}\left(-j\right)^{n}\frac{\beta_{n}}{n!}\frac{\partial^{n}A}{\partial T^{n}}=j\gamma\left|A\right|^{2}A \tag{2.1}$$

where β_n is the Taylor series of the wavenumber $\beta(\omega)$, $T = t - \beta_1 z$, A is a time variable in the reference frame of the slowly varying envelope of the pulse; α is the attenuation coefficient, and γ is the nonlinear coefficient of the fiber [19]. As mentioned before, one of the important properties of the fiber, discussed extensively in this dissertation, is chromatic dispersion. In this dissertation, the effect of CD has been either utilized or mitigated, and we elaborate on it in the following section.

2.2.1. Chromatic Dispersion

In general, the dielectric medium response to an electromagnetic wave excitation is in general frequency-dependent. On a macro-scale, this feature manifests itself as the frequency dependence of the refractive index, $n(\omega)$, and is referred to as chromatic dispersion. As is well known [20], a waveguiding structure supports only a finite number of electric field configurations (that can be transported, or guided by the structure). In consequence to the frequency dependence of the refraction index, the (so-called) wavenumber or mode-propagation constant, β, of the optical wave traveling through a dielectric medium, is related to the dielectric refractive index as [19]:

$$\beta\left(\omega\right)=n\left(\omega\right)\frac{\omega}{c_{0}} \tag{2.2}$$

where c_0 is the speed of light in vacuum, i.e., $c_0 = 299{,}792{,}458$ m/s .

To study the effect of dispersion in pulse propagation through fibers, it is convenient to expand $\beta(\omega)$ in a Taylor series about the center frequency ω_0:

$$\beta(\omega) = \beta_0 + \beta_1(\omega-\omega_0) + \frac{1}{2}\beta_2(\omega-\omega_0)^2 + \frac{1}{6}\beta_3(\omega-\omega_0)^3 + \frac{1}{24}\beta_4(\omega-\omega_0)^4 + \ldots \qquad (2.3)$$

where

$$\beta_m = \left(\frac{d^m\beta}{d\omega^m}\right)_{\omega=\omega_0} \qquad (\mathrm{m} = 0, 1, 2, \ldots) \; . \qquad (2.4)$$

Are denoted dispersion coefficients of order m (with respect to frequency). In the applications discussed in this thesis, the effects of up to the fourth-order dispersion of the fiber, β_4 term, are taken into account, whereas the higher-order terms were found to be immaterial and have, thus, been neglected in our considerations.

The first and second terms of the $\beta(\omega)$ have special physical implication: Namely, the pulse envelope moves at the group velocity, v_g, and β_1 is the inverse of the group velocity

$$\beta_1 = \frac{d\beta}{d\omega} = \frac{1}{v_g} \qquad (2.5)$$

with units of [s/m]. Correspondingly, the β_2 captures the linear change of the β_1 parameter with frequency and is responsible for pulse broadening [19]. Fittingly, the β_2 parameter bears the name of Group-Velocity Dispersion (GVD) and is expressed in units of [s^2/m] in the SI system of units.

$$\beta_2 = \frac{d^2\beta}{d\omega^2} \qquad (2.6)$$

In some applications, it is more convenient to consider dispersion as a function of wavelength. Considering the relation

$$\beta(\omega)\,d\omega = D(\lambda)\,d\lambda \tag{2. 7}$$

the dispersion parameter D and the dispersion slope S with typical units of [ps/nm/km] and [ps/nm^2/km], respectively, are defined as

$$D(\lambda) = \frac{d\beta_1}{d\lambda} = \frac{-2\pi c_0}{\lambda^2}\beta_2(\omega_0) \tag{2. 8}$$

$$S(\lambda) = \left(\frac{2\pi c}{\lambda^2}\right)^2 \beta_3(\omega_0) - \frac{2}{\lambda}D(\lambda). \tag{2. 9}$$

In optical communication applications, usually only the second order, β_2, term is of importance (and consideration), whereas the higher-order terms are neglected. To study pulse propagation in a dispersive fiber, we consider Eq. 2.1 in the absence of nonlinearity and attenuation:

$$\frac{\partial A}{\partial z} + j\frac{1}{2}\beta_2\frac{\partial^2 A}{\partial T^2} = 0. \tag{2.10}$$

If $\tilde{A}(z,\omega)$ is the Fourier transform of $A(z,T)$ such that

$$A(z,T) = \frac{1}{2\pi}\int_{-\infty}^{\infty}\tilde{A}(z,\omega)e^{j\omega T}\,d\omega \tag{2. 11}$$

Then the solution to Eq. 2.10 in the frequency domain can be readily found by taking the Fourier transform of the Eq. 2.11:

$$\frac{\partial \tilde{A}}{\partial z} - j\frac{1}{2}\beta_2\omega^2\tilde{A} = 0 \tag{2. 12}$$

and the solution to this ordinary differential equation is:

$$\tilde{A}(z,\omega) = \tilde{A}(0,\omega)\exp\left(-j\frac{1}{2}\beta_2\omega^2 z\right). \tag{2. 13}$$

Therefore, a dispersive fiber introduces a quadratic spectral phase shift or a chirp in the frequency domain. In the following, the optical coherent detection concept is explained and the effect of this quadratic spectral phase shift in the time domain will be discussed.

2.3.Coherent Optical Transmission

As the immense growth of global data traffic pushes optical communication systems toward higher spectral efficiency (defined as R/B for the information rate R transmitted over a specific bandwidth B having units of [bits/s/Hz] [21]), the coherent optical communication systems have attracted a lot of attention in both research and industry communities. In these systems, the information is encoded in both the amplitude and phase of the optical carrier or real (I) and imaginary (Q) part of the electrical field, using an IQ modulator as shown in Figure 2. 1. Moreover, the coherent optical detection is polarization-sensitive so the state of polarization (SOP) of the electrical field is also used to encode and convey the information in coherent communication systems.

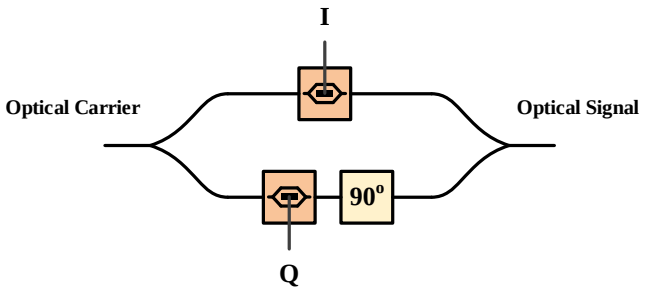

Figure 2. 1 IQ Modulator or nested Mach-Zehnder Modulator (MZM) which consists of an MZM in each arm. The two arms are offset in phase by 90°, setting them in quadrature to each other.

Nonetheless, this higher spectral efficiency in coherent optical systems is achieved at the expense of higher implementation complexity, comparing to the Intensity Modulation and Direct

Detection (IMDD) systems, shown in Figure 2. 2, wherein the information is encoded and retrieved from only the intensity of the electrical field.

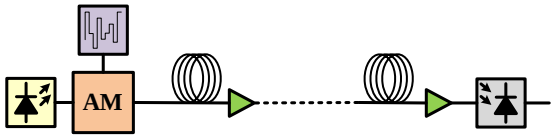

Figure 2. 2 IMDD system which uses intensity-only modulation and the intensity of the optical field transmitted through the optical fiber link is detected by a photodiode acting as a square-law detector [22].

Besides that, the optical coherent systems are sensitive to random fluctuations of the SOP and the carrier phase [22]. Nevertheless, these can be digitally mitigated in the receiver (in digital coherent transmission systems) by means of digital signal processing (DSP), as explained in sections 2.3.2 and 2.4. In the following, the principle of coherent detection and the retrieval of the complex electric field is discussed.

2.3.1. Coherent Detection

In coherent receivers, a balanced photo-detector , in the configuration as shown in Figure 2. 3, is utilized to capture the beat between the modulated signal light and the Continuous-Wave (CW) Local Oscillator (LO). Balanced receivers consist of anti-parallel photodiodes and have the potential to suppress the relative intensity noise (RIN) and the common mode noise (e.g. amplified spontaneous emission noise (ASE) from erbium-doped fiber amplifiers [23]). Assume that the SOP of the signal and LO are perfectly aligned by a Polarization Controller (PC). Assuming the complex electric field of the received signal is

$$S(t) = A_s(t)e^{j\omega_s t} \tag{2.14}$$

whilst, the LO is given by

$$L(t) = A_l e^{j\omega_l t} \tag{2.15}$$

The outputs of the 50:50 coupler in Fig. 2.3 are

$$E_1 = \frac{1}{\sqrt{2}}\left(S(t) + L(t)\right) = \frac{1}{\sqrt{2}}\left(A_s(t)e^{j\omega_s t} + A_l e^{j\omega_l t}\right) \tag{2.16}$$

$$E_2 = \frac{1}{\sqrt{2}}\left(S(t) - L(t)\right) = \frac{1}{\sqrt{2}}\left(A_s(t)e^{j\omega_s t} - A_l e^{j\omega_l t}\right) \tag{2.17}$$

And are detected by a square-law photodetector with a responsivity of $\Re$, wherein the output current is proportional to the time-averaged magnitude-squared of the electric filed $\left(I(t) \propto \Re < |e(t)|^2 >\right)$. In homodyne detection, i.e., $\omega_s = \omega_l$, the output currents of the two photodetectors are

$$I_1(t) \propto \Re\left(\left|A_s(t)\right|^2 + \left|A_l\right|^2 + 2\,\mathrm{Re}\left(A_s(t)A_l^*\right)\right) \tag{2.18}$$

$$I_2(t) \propto \Re\left(\left|A_s(t)\right|^2 + \left|A_l\right|^2 - 2\,\mathrm{Re}\left(A_s(t)A_l^*\right)\right). \tag{2.19}$$

Therefore, the output current of the balanced receiver is:

$$I(t) = I_1(t) - I_2(t) \propto \Re\,\mathrm{Re}\left(A_s(t)A_l^*\right) \tag{2.20}$$

which gives the beat between the signal and the LO.

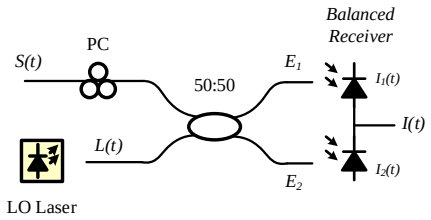

Figure 2. 3 Balanced Receiver used to measure the beat between the signal *S*(t) and LO.

As Eq. 2.20 implies, the balanced receiver acts like an RF mixer and can be utilized to restore the full information of the transmitted complex electrical field by using a 90° Hybrid as shown in Figure 2. 4. The 90° phase shift in one arm of the hybrid and the optical field mixing in the balanced receiver results in the detection of both I and Q components of the optical signal.

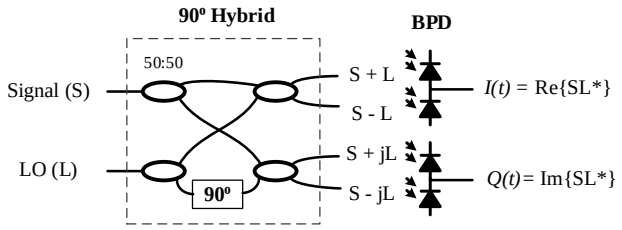

Figure 2. 4 Optical Coherent Receiver which retrieves the real (I) and imaginary (Q) components of the electric field.

2.3.2. Figure of Merit for the Detected Digitally Modulated Optical Signal

One of the most important tasks in optical communication is the assessment of the integrity of the detected optical signal, which reflects the quality and reliability of the transmission system [24]. Consider the simplest Quadrature Amplitude Modulation (QAM), i.e., 4-QAM or QPSK, in which two bits are encoded into each transmitted symbol, thus the total number of possible symbols is $2^2 = 4$. Figure 2.5(a) shows the distribution of these four symbols in the complex plane for a QPSK optical signal. This graphical representation of the symbols is called a constellation diagram.

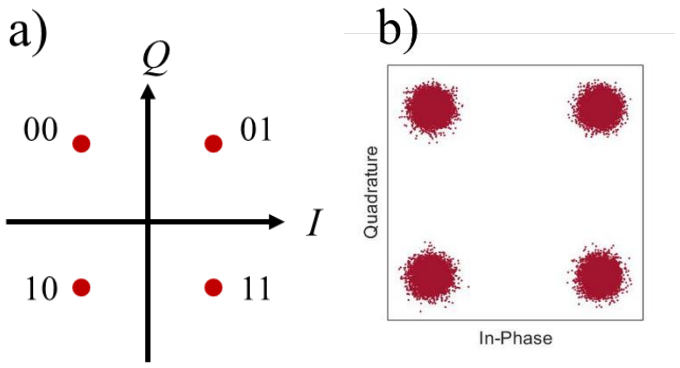

Figure 2. 5 Constellation diagram. a) Ideal QPSK signal. b) QPSK signal in a realistic optical communication system.

In an ideal QAM signal, each symbol is represented by a unique location in the constellation diagram, as shown in Figure 2.5(a). Yet, in practice (i.e. in real-life communication systems), the noise and other impairments distort the signal and force these points to deviate from their ideal intended location. Even in the generated and transmitted QPSK optical signal, these points have a cloud-like distribution like those shown in Figure 2.5b. Thus, the constellation diagram itself can serve as a visual representation enabling some basic intuitive insight into the integrity and quality of the received optical signal. In the strict sense, however, the deviation of the constellation points is directly related to the amount of noise and distortion. Thereby, when these impairments are strong, the original constellation point is displaced far enough from its ideal location such that it can wonder off into the vicinity of the constellation point of another symbol, obviously causing an error in the detection process at the receiver (e.g. a transmitted “01” bit combination, which after encoding is represented by a symbol from the upper right corner of the constellation diagram in Fig. 2.5, may be detected, or mis-interpreted as the “11” symbol, etc.).

While the Bit-Error Rate (BER), i.e., the rate of bit-errors occurring in the transmission system, is the ultimate quality measure of the communication signal, in simulations and off-line

signal processing counting errors becomes time-consuming and impractical – especially in the case of low BERs. Thus, it is more reasonable to estimate the BER [24]. One of the popular metrics for evaluating the quality of the optical signal in practice is the Quality-Factor (QF), which is related to BER [21], [25] through the complement error function. When the signal is distorted by Additive White Gaussian Noise (AWGN), the QF is given by

$$Q = \sqrt{2} erfc^{-1}\left(2BER\right) \tag{2.21}$$

where $erfc^{-1}$ is the inverse of the complementary error function. Moreover, the QF implies how noisy the constellation diagram is. For high QF, the clouds of the constellation points are denser and far from each other. This property can be inferred from the original definition of QF related to binary IMDD communication, which is characterized by signal-dependent Gaussian noise:

$$Q = \frac{r_1 - r_2}{\sigma_1 + \sigma_2} \tag{2.22}$$

where r_i is the mean value of the cloud, and σ_i is the standard deviation.

2.3.3. Digital Coherent Transmission Systems

The utilization of digital signal processing (DSP) in high-speed optical fiber communication systems has been enabled by the emergence of data converters with a speed commensurate with the optical data rate over the last decade. It was the combination of coherent detection, high spectral efficient modulation formats, and DSP that led to the development of high capacity digital coherent optical communication systems supporting the current 100GbE [26].

The configuration of a digital coherent optical transmission system, from the transmitter to the receiver, is shown in Figure 2. 6. The system is designed to be phase and polarization-sensitive,

thus, supporting the transmission of polarization division multiplexing QAM (PDM-QAM) optical signals.

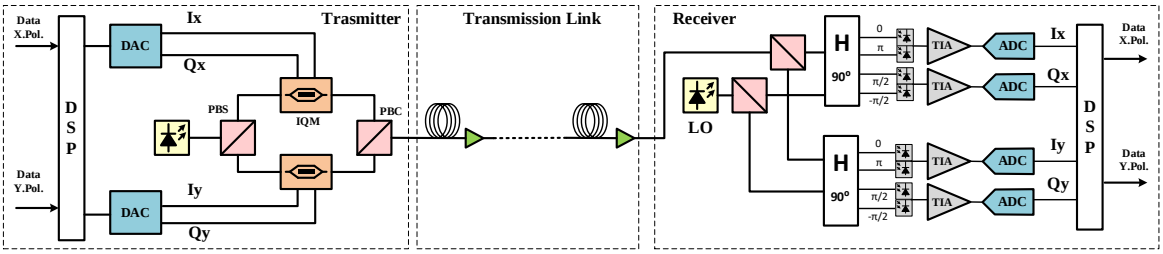

Figure 2. 6 Configuration of a digital coherent optical transmission system.

At the transmitter, in the most straightforward scenario, first, two independent sequences for the x- and y-polarization are processed at the DSP. The DSP chain in the transmitter and the receiver will be discussed in section 2.4. The resulting digital data is converted to an analog signal using two Digital-to-Analog Converters (DACs) for each x- and y-polarization. The two outputs of each DAC, the I and Q signal of the QAM modulation format, drive an IQ modulator. The output of a single CW laser is split by a Polarization Beam Splitter (PBS) and serves as the optical carrier for the two IQMs. Finally, the output of the two IQMs is combined using a Polarization Beam Combiner (PBC). The generated optical QAM signal is transmitted through an optical fiber link. Erbium-Doped Fiber Amplifiers (EDFAs) are periodically placed in the transmission link to account for the propagation losses in the link. At the receiver, the received optical signal and the output of the LO laser are each split into two orthogonal x- and y-polarizations using PBS. Then, each x- and y-polarization is coherently detected using a coherent receiver as shown in Figure 2.4 and 2.6. Then, the detected signal is amplified using a Trans-Impedance Amplifier (TIA), converted into digital using an Analog-to-digital Converter (ADC), and finally processed and demodulated in the DSP chain of the receiver.

2.4.Digital Signal Processing

The most common DSP chain in coherent transmitter and receiver is shown in Figure 2.7. At the transmitter, first, the binary sequence is mapped into the corresponding complex symbol. Then, the pulse shaping filter is applied mainly to restrict the spectral bandwidth of the modulated signal. The final block of the transmitter DSP chain is the correction of any imperfection, i.e., nonlinearity and frequency roll-off, of the electronic and optical components. For example, the nonlinearity of MZM could be digitally pre-compensated in this step.

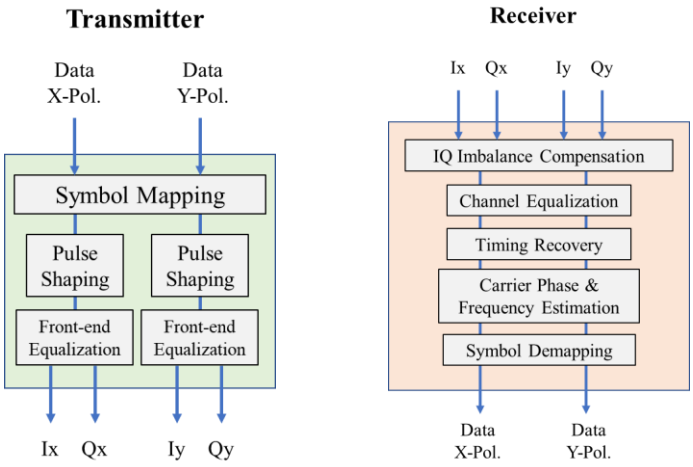

Figure 2. 7 DSP chain in coherent transmitter and receiver.

The received signal is contaminated by noise and transmission link- (or channel) impairments. The linear effects of the fiber such as chromatic dispersion, polarization mode dispersion (PMD), and polarization mode loss, in addition to the nonlinear effects such as self-phase modulation, cross-phase modulation (XPM), and four-wave mixing (FWM) may be the source of the transmission impairment [26].

The first block in the receiver DSP chain compensates for any amplitude, phase, or timing error between the I and Q component of the complex signal. Then, the linear and nonlinear channel impairments are digitally equalized. In the next step, the timing errors are estimated and corrected to guarantee the waveforms are sampled at the correct points. Following, the laser phase noise and the frequency mismatch between the LO and transmitting laser are estimated and compensated in the carrier recovery block. One of the important advantages of phase-sensitive coherent receivers over direct detection is in circumventing the need for an optical phase-locked loop (OPLL) for phase synchronization [26]. The M^{th} power [27] and blind search algorithms [28] are the most common Carrier Phase Estimation (CPE) algorithms. Lastly, the transmitted symbols are estimated.

2.4.1. Digital Chromatic Dispersion Compensation

As mentioned in section 2.2.1 and shown in Eq. 2. 13, pulses propagating through a dispersive fiber acquire quadratic spectral phase shift. This quadratic phase or frequency-dependent delay means that different parts of the pulse spectrum propagate with different speeds through the fiber. As a result, pulse broadening will occur. A graphical representation of this effect is shown in Figure 2.8. As transmitted pulses change shape and are broadened in the time domain, the interference of the neighboring pulses might dramatically change the pulse shape and cause an error in symbol de-mapping at the receiver. This effect is referred to as inter-symbol interference (ISI).

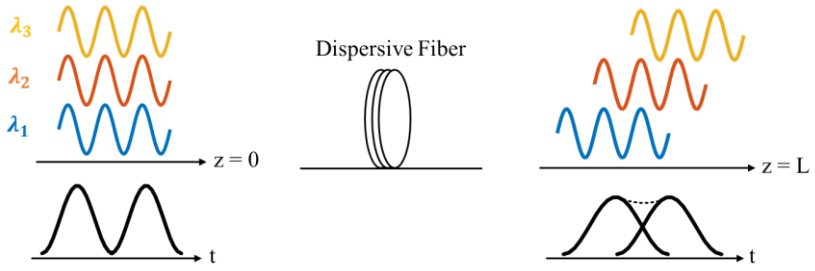

Figure 2. 8 Graphical representation of chromatic dispersion effect in fiber: different wavelengths travel with different speeds which results in pulse broadening in time-domain and inter-symbol interference.

To illustrate the effect of CD on the quality of the optical signal, using MATLAB software, we have simulated the transmission of the 16-QAM optical signal through a single-mode fiber (SMF) with a dispersion parameter of D = 17 ps/nm/km and zero dispersion slope, in absence of attenuation and nonlinearity. The baud rate or symbol rate of the signal was 100 Gigabaud (GBd). The constellation diagram of the signal for different transmission lengths is shown in Figure 2.9, assuming that an ideal 16-QAM signal was generated and transmitted through the fiber. As the signal travels through the fiber, it becomes more and more distorted. So that, we have a totally distorted signal, shown in Figure 2.9, at the transmission length of 4km.

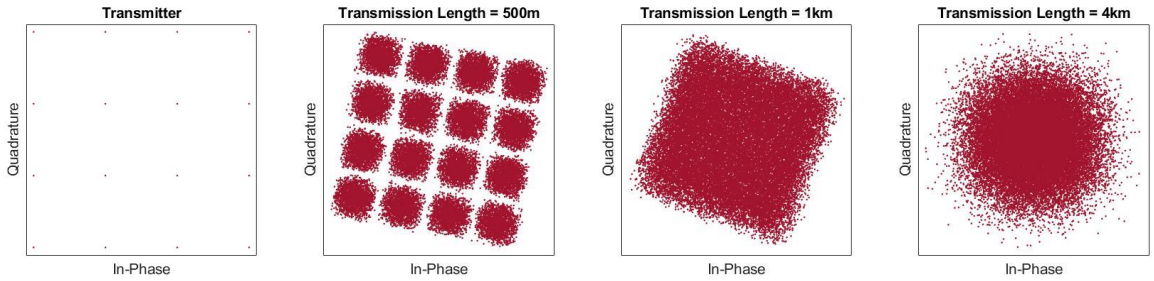

Figure 2. 9 Constellation diagram of 100GBd 16-QAM signal transmitted through an SMF at different transmission lengths.

As Eq. 2.13 shows, the transfer function of the CD is given by

$$G(z,\omega)=\exp\left(-\frac{j\omega^2\beta_2 z}{2}\right) \tag{2.23}$$

Therefore, the dispersion compensating filter should be an all-pass filter with the transfer function $H_c(\omega)=1/G(z,\omega)=G(-z,\omega)$. This is one of the digital filters implemented in the channel equalization block of the DSP chain shown in Figure 2.7.

The dispersion compensating filter can be implemented using the frequency domain methods [29]. It can also be approximated in the time domain using a Finite Impulse Response (FIR) filter [30]. The impulse response of the CD compensating filter, $h_c(t)$, is given by the inverse Fourier transform of the $H_c(\omega)=G(-z,\omega)$ as:

$$h_c(z,t)=\frac{1}{\sqrt{-2\pi j\beta_2 z}}\exp\left(-j\frac{t^2}{2\beta_2 z}\right). \tag{2.24}$$

However, to implement this filter in the digital domain, it should have a finite length. Besides that, since it passes all frequencies, the aliasing will occur for a finite sampling frequency. Therefore, the corresponding finite impulse response filter is truncated to N taps with tap weights given by:

$$h_n=\sqrt{\frac{jc_0T^2}{D\lambda^2 z}}\exp\left(-j\frac{\pi c_0T^2}{D\lambda^2 z}k^2\right),\quad -\left[\frac{N}{2}\right]\le k\le\left[\frac{N}{2}\right]\ \text{ and }\ N=2\times\left\lfloor\frac{|D|\lambda^2 z}{2c_0T^2}\right\rfloor+1. \tag{2.25}$$

An FIR filter is a filter whose impulse response is of finite duration. As shown in Figure 2. 10, the output of an FIR filter is a weighted sum of the delayed replicas of the input. It should be noted that the relative delay between taps in this filter is constant.

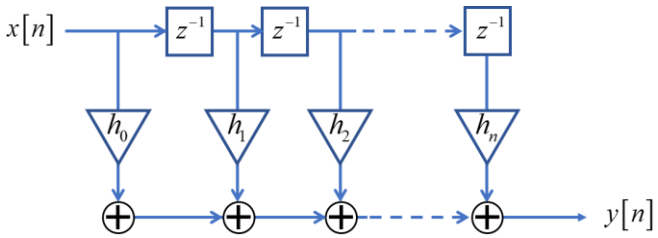

Figure 2. 10 Block diagram of an N-tap FIR filter.

The chromatic dispersion effect in optical fibers, which is the dominant detrimental effect in optical coherent communication, has been beneficial in the FIR RF-photonic filter implementation discussed in chapter 3. It was the dispersion or frequency-dependent delay of the fiber that defined the relative delay between the tap coefficients of our implemented RF-photonic filter.

Chapter 3 Sub-GHz Flat-top Comb-based RF-Photonic Filter Enabled by Fourth-order Dispersion Compensation

3.1. Introduction

RF-photonics has attracted the attention of both the research community and the commercial sector in recent years. In particular, RF-photonic subsystems take advantage of characteristics inherent to photonics to carry out functionalities that might be very difficult, or even impossible by RF subsystems alone [31]. Namely, optical fibers due to their low weight, cost, and propagation loss, as well as the inherent immunity to interference are an ideal transport platform for high-bandwidth RF signals over nearly unlimited lengths [1]. Additionally, optical fibers offer ample processing bandwidth to RF signals upconverted to photonic frequencies [32]. Moreover, the flexibility in manipulating the overall link response is one of the key reasons to adopt the photonic-aided subsystems over the conventional RF systems. In fact, the programmability and frequency-tunability over the GHz range are the two most prominent attributes of RF-photonic filters. While frequency-tunable RF filters have been implemented using various tuning elements such as yttrium iron garnet (YIG) resonators, RF microelectromechanical systems (MEMS), and semiconductor varactor diodes, the RF-photonic-based filters outperform those by offering simultaneous high-speed frequency tuning over a wide frequency range, low control voltage, and linear relationship between the filter frequency and control voltage [33]. It is important to emphasize that these features might manifest their significance in the 5G communication network, which covers different frequency bands [34]. For example, in the latter application, the RF-photonic solution may be conducive to providing a single frequency-tunable and shape-

programmable RF-Photonic filter for wireless base stations, which otherwise require equipping with several protocol-specific filters, thus offering a more than adequate alternative.

Numerous schemes have been proposed and demonstrated in the past for the implementation of RF-photonic filters and particularly the multitap delay line FIR filters, having a broad potential due to their flexibility and reconfigurability. In the earlier implementations, the RF signal was modulated directly onto a continuous wave laser source, then demultiplexed into several physical delay lines, each acting as a tap coefficient. In these filters, the coefficients' amplitude was set by controlling the attenuation in each of the delay line elements. The output was then multiplexed together and passed to the photodetector [35]. The main drawbacks of this scheme pertain to the difficulty in scaling the number of filter taps, as well as to the filter frequency tuning. To circumvent these constraints, FIR RF-photonic filters based on multiwavelength sources, followed by dispersive element(s) have been adopted, wherein each comb line (i.e., the frequency tone) is used as a filter tap coefficient, whereas a dispersive element is utilized to impose the relative delay between the taps. In particular, these implementations have benefited from the utilization of the Pulse Shaper device, which enables precise control of the amplitude and phase of each coefficient [36] and hence flexible programming of the filter magnitude and phase responses that are of primary importance for an accurate filter realization. In addition, the previous implementations benefited from the utilization of a dispersive fiber or chirped fiber Bragg gratings (CFBG) serving as dispersive elements, while arrays of CW lasers [37], mode-locked lasers [38], spectrally-sliced [39] and contiguous [40] noncoherent broadband optical sources (BOS), or electro-optic (EO) frequency combs [41] have been used as a multi-wavelength source(s). Among these, noncoherent broadband optical sources and EO combs have been the two preferred choices in the most prominent prior RF-photonic filter realizations. While the BOS-based filters have been

studied extensively due to their cost-effectiveness and scalability to a large number of taps, the lack of coherency, as well as the low power spectral density associated with this type of source, limit the filter application and capability. In contrast, the optical comb-based RF-photonic filters offer a considerably enhanced noise resilience and more efficient use of optical bandwidth (as compared to the noncoherent BOS-based counterparts [42]).

In the realization of the RF-photonic filters based on multi-wavelength sources and dispersion, the dispersion profile of the dispersive element over the relevant optical bandwidth is another determining factor in RF-photonic filters characteristics. In fact, in FIR RF-photonic filters whose implementation is based on multicarrier sources and dispersive elements, the required relative delay between the filter taps is defined by the quadratic phase introduced by the dispersive fiber [41]. Consequently, a departure of the waveguide dispersion from linearity with respect to frequency (or, as is often referred to - the presence of higher-order dispersion terms in the waveguide characteristic) will necessarily lead to the departure from the designed response and the distortion in the filter shape. Furthermore, it is self-explanatory that the effect of non-ideal dispersive characteristic will be even more harmful in the case of wide-band optical sources [43]. Worse yet, this distortion is bound to become even more prominent with filter tuning [44]. Accordingly, in order to construct a narrow (i.e., sub-GHz), or a tunable shape-invariant filter, it is absolutely critical to maintain tight control of the higher-order dispersion in the dispersive waveguide. The impact of Third Order Dispersion (TOD) on RF-photonic filters has been studied extensively and several schemes have been implemented to mitigate this effect. In [43], a cascade of SMF and dispersion compensating fiber (DCF) were used to attempt to cancel the overall higher-order dispersion. Similarly, a CFBG was utilized to cancel TOD in DCF [45]. Alternatively,

a pulse shaper was used to cancel the TOD terms, in [46], [47]. Despite the comprehensive study on the TOD mitigation in RF-photonic filters, fourth-order dispersion in dispersive fiber has scarcely been encountered and discussed in the prior work. The only such example, to the best of our knowledge, is related to the encounter of a 50 nm bandwidth optical source in [43], where the fourth-order dispersion was determined to be causing the higher frequency sidelobe in the filter response. However, no attempt was made to cancel the distortion in that work.

On the other hand, the ability to extract an arbitrary-width RF content at any frequency is the enabling part of advanced receivers. However, despite this widely recognized role, practical RF-photonic filters have been constrained to selectable bandwidth. For instance, RF-photonic filters have been implemented for applications such as phase filtering for pulse compression [48], [49], or dynamic filtering of frequency-hopped and chirped RF signals [3]. Furthermore, virtually all RF signals are implemented in some guise of Nyquist shaping. Yet very few previous demonstrations of the RF-photonic filters have exhibited a flat-top RF spectral shape required for Nyquist-shaped waveforms. Additionally, the bandwidth of the reported comb-based flat-top filters has almost universally exceeded 1.5 GHz [33], [50], [51], which is of very little practical interest since the RF applications rarely occupy more than GHz of bandwidth [52], [53]. Considering these restrictions, we have demonstrated the first sub-GHz RF-photonic filter based on an all-fiber parametric comb, enabled by the compensation of the fourth-order dispersion in the delay line element. The filter integrity was further tested and verified by retrieving a set of digital modulated RF channels asserting its outstanding quality. The remaining part of this chapter is organized as follows. Section 3.2 lays out the theory of the higher-order dispersion compensation for the implemented RF-photonic filter. Details of the experimental setup are provided in section

3.3. In Section 3.4, experimental results including filter transfer function, filter tuning, and RF channels retrieval are presented. The results are summarized in Section 3.5.

3.2.Theory

As directly implied by Fourier analysis, the filters with narrow bandwidth, sharp transition (i.e., edges in the frequency domain), and higher main-to-side-lobe suppression require a larger number of taps, and thus an increased number of comb lines. While utilizing a higher number of comb lines might seem like a promising approach for a narrower bandwidth implementation, reliance on a wider optical bandwidth comes with its own set of issues, among which, mitigation of higher-order dispersion of the dispersive element becomes the primary concern.

As will be illustrated in the experimental results, the 45 nm bandwidth of the utilized optical comb in our experiment was wide enough to incur significant impairments (and thus distortions and departure from the desired filter shape) due to not only third but also fourth-order dispersion in the dispersive element. In the following, we derive the expression conducive to higher-order dispersion compensation, relevant to the experimental setting implemented.

A typical high-level configuration for the generation of an RF-photonic filter capable of higher-order dispersion compensation in the dispersive element is shown in Figure 3.1. The wide-band source is passed through the pulse shaper #1 to imprint the time-domain amplitude filter coefficients onto the comb lines. The electric field after the Pulse Shaper can be expressed as:

$$E(t) = \sum_n e_n(t) = \sum_n \sqrt{P_n} e^{j\Omega_n t} e^{j\phi_n} + c.c. \quad (3.1),$$

where P_n corresponds to the power of each comb line and $\Omega_n = \Omega_0 + n\Delta\Omega$, represents the (angular) frequency of each of the comb lines, with $\Delta\Omega$ being the comb frequency pitch (in rad/s). As is well known, the absolute phase of the comb lines, ϕ_n, does not affect the overall filter transfer function whereas only the phase difference between the two arms of the interferometer plays a note-worthy role [41]. Consequently, the ϕ_n can be altogether neglected in the following equations.

Following the Pulse Shaper, the shaped tones are split into two interferometric arms to provide for the carrier and side-band signal modulation [54]. The fraction of the power directed in the lower arm of the interferometer (modulator arm) is α, for the α:1-α input power split ratio of the interferometer.

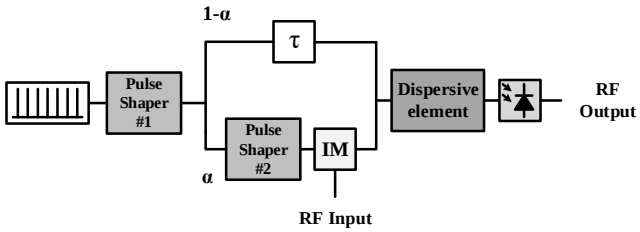

Figure 3. 1 The setup for higher-order dispersion compensation in dispersive element in RF-photonic flat-top filter generation (IM: Intensity Modulator and α:1-α is the input power split ratio of the interferometer).

A flat-top filter, having a sinc-like profile in the time domain necessarily needs to support tap coefficients of both positive and negative signs. Therefore, a second pulse shaper is required to regulate, or impose the phase of the respective filter taps. We additionally note that the phase applied by this pulse shaper could be also used to implement the wide bandwidth higher-order dispersion compensation. Although apparently, the most flexible, the utilization of the second pulse shaper does not come about without its own issues. Specifically, the phase modulation depth and finite frequency resolution (i.e., 10 GHz for the unit used in our experiments) of the device

limits the ability to compensate the phase with arbitrary accuracies. Consequently, taking into account the practical device limitations, the intra-interferometer placement of the pulse shaper has been recognized as the most practical experimental configuration for higher-order dispersion compensation. Therefore, the pulse shaper #2 in the lower interferometric arm is considered to regulate the tap phase. The amplitude and phase apodized comb is then double-sideband modulated in an electro-optic intensity modulator driven by the input RF signal. A Variable Delay Line (VDL) in the upper arm of the interferometer is used to vary the filter center frequency. Considering the time delay, τ, imposed by the VDL and the double-sideband modulation in the lower arm of the interferometer, the electric field corresponding to the nth comb line after the interferometer can be expressed as:

$$e_n(t) \propto \sqrt{P_n} e^{j\Omega_n t} \left\{ e^{-j\tau\Omega_n} - \frac{j\pi v_{RF}}{2v_\pi} \sqrt{\frac{\alpha}{1-\alpha}} \sin(\omega t) e^{j\psi_n} \right\} + c.c. \quad (3.2),$$

by taking the small-signal approximation for the input RF signal [54], where ψ_n is the phase applied to each tap by the intra-interferometer pulse shaper, v_π is the half-wave voltage of the modulator, and ω and v_{RF} are the frequency (in rad/s) and the maximum voltage of the input RF signal, respectively. As previously noted, the relative time delay between the filter taps is produced by the dispersive element inserted after the interferometer. In this analysis, up to its fourth-order dispersion is taken into consideration. Thus, the phase introduced by the dispersive element is:

$$\Phi(\Omega) = \theta_0 + \theta_1(\Omega - \Omega_0) + \frac{1}{2}\theta_2(\Omega - \Omega_0)^2 + \frac{1}{6}\theta_3(\Omega - \Omega_0)^3 + \frac{1}{24}\theta_4(\Omega - \Omega_0)^4 \quad (3.3),$$

where $\theta = -\beta L$, β is the propagation constant and L is the length of the dispersive element. Consequently, the electric field at the input of the photodetector is given by:

$$e_n(t) \propto \sqrt{P_n} e^{j\Omega_n t}\left\{e^{-j\tau\Omega_n} e^{j\Phi(\Omega_n)} - Ae^{j\omega t} e^{j\Phi(\Omega_n+\omega)} e^{j\psi_n} + Ae^{-j\omega t} e^{j\Phi(\Omega_n-\omega)} e^{j\psi_n}\right\} + c.c. \tag{3.4}$$

where $A = \frac{\pi v_{RF}}{4v_\pi}\sqrt{\frac{\alpha}{1-\alpha}}$. On the other hand, the current at the output of the photodetector is proportional to the time-averaged magnitude-squared of the electric field ($i(t) \propto \Re\left\langle \left|e(t)\right|^2 \right\rangle$ where $\Re$ is the responsivity of the photodetector). If we define the filter transfer function as the ratio of the output voltage and the system input voltage, the transfer function can be expressed as:

$$\begin{aligned} H(\omega) \propto & \sum_n P_n e^{-j\tau\Omega_n} e^{-j\Psi_n} e^{j[\Phi(\Omega_n)-\Phi(\Omega_n-\omega)]} \\ & - \sum_n P_n e^{j\tau\Omega_n} e^{j\Psi_n} e^{j[\Phi(\Omega_n+\omega)-\Phi(\Omega_n)]} \end{aligned} \tag{3.5}$$

We refer to the first and second terms on the right side of Eq. 3.5 (namely the upper and the lower sidebands) as $H_-(\omega)$ and $H_+(\omega)$, respectively. Based on Eq. 3.3 and Eq. 3.5, the two sidebands can be expressed as:

$$H_- \propto \sum_n P_n e^{-j\tau(n\Delta\Omega)} e^{-j\Psi(\Omega_n)} exp\left(j\left((n\Delta\Omega)(\theta_2\omega - \tfrac{1}{2}\theta_3\omega^2 + \tfrac{1}{6}\theta_4\omega^3) + (n\Delta\Omega)^2(\tfrac{1}{2}\theta_3\omega - \tfrac{1}{4}\theta_4\omega^2) + \tfrac{1}{6}(n\Delta\Omega)^3\theta_4\omega\right)\right) \tag{3.6}$$

$$H_+ \propto \sum_n P_n e^{+j\tau(n\Delta\Omega)} e^{j\Psi(\Omega_n)} exp\left(j\left((n\Delta\Omega)(\theta_2\omega + \tfrac{1}{2}\theta_3\omega^2 + \tfrac{1}{6}\theta_4\omega^3) + (n\Delta\Omega)^2(\tfrac{1}{2}\theta_3\omega + \tfrac{1}{4}\theta_4\omega^2) + \tfrac{1}{6}(n\Delta\Omega)^3\theta_4\omega\right)\right). \tag{3.7}$$

Lastly, recognizing the filter bandwidth to be much smaller than its center frequency, $BW \ll \omega_f$, where ω_f is filter center frequency, we can safely assume $\omega \approx \omega_f$. Therefore, Eqs. 3.6 and 3.7 readily offer the sought-after expression for the higher-order dispersion compensation. To further simplify the expression, we express the resulting phase in a parameterized form as:

$$\Psi(\Omega_n) = \varphi_n + A_n(n\Delta\Omega) + B_n(n\Delta\Omega)^2 + C_n(n\Delta\Omega)^3 \tag{3.8}$$

where φ_n is the phase of the time-domain filter coefficients. Hence, the parameters A_n , B_n and C_n used for the purpose of dispersion compensation are as follows:

$$A_n = -\frac{1}{2}\theta_3\omega_f^2 + \frac{1}{6}\theta_4\omega_f^3, \quad B_n = \frac{1}{2}\theta_3\omega_f - \frac{1}{4}\theta_4\omega_f^2, \quad C_n = \frac{1}{6}\theta_4\omega_f \tag{3.9}$$

for the H_- and

$$A_n = -\frac{1}{2}\theta_3\omega_f^2 - \frac{1}{6}\theta_4\omega_f^3, \quad B_n = -\frac{1}{2}\theta_3\omega_f - \frac{1}{4}\theta_4\omega_f^2, \quad C_n = -\frac{1}{6}\theta_4\omega_f \tag{3.10}$$

for the H_+ band.

It is also worth noting that, in sharp contrast to the RF-photonic filters relying on noncoherent BOS in which the applied correction phase needs to be continuous, in filters relying on frequency combs, the needed correction can be performed discretely – i.e., solely in the vicinity of the comb-line carrying tap coefficients. This both simplifies the task at hand and is certainly more appropriate considering the inherent finite resolution of the pulse shaper device.

The details of our experimental setup are presented in the following.

3.3.Experimental Setup

The experimental setup used to generate and characterize a sub-GHz flat-top RF-photonic filter is shown in Figure 3.2. The multiwavelength source was a 25 GHz-pitched all-fiber parametric comb seeded by a CW laser at 1549.3 nm and Optical Signal-to-Noise Ratio (OSNR) of 59.6 dB, at 0.1 nm resolution. In contrast to conventional, cavity-based combs, the parametric comb operates in a traveling-wave regime, generating new frequencies from the seed master oscillator launched into the multi-segment shock-wave parametric mixer [16]. Specifically, the

compressor stage in the shock-wave mixer is designed to increase the efficiency of the four-wave mixing process by generating shock waves with high peak power [55].

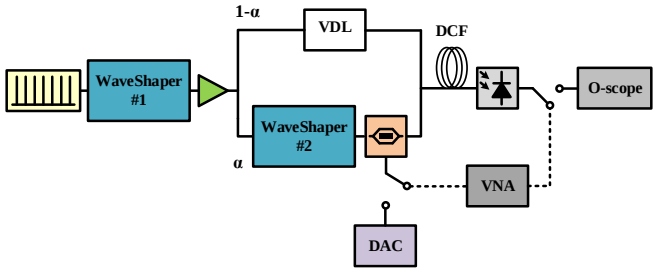

Figure 3. 2 Experimental setup of RF-photonic sub-GHz flat-top filter, wherein the modulator was driven by two different sets of RF signals. First, a VNA was used to characterize the filter transfer function. Once the desired filter response was achieved by programming the waveshaper #2, the effectiveness of the filter was tested on a set of digital modulated RF signals generated by a DAC and detected by oscilloscope.

The spectrum of the generated source is shown in Figure 3.3. This wideband parametric comb was characterized by an OSNR of 45 dB at 0.1 nm resolution.

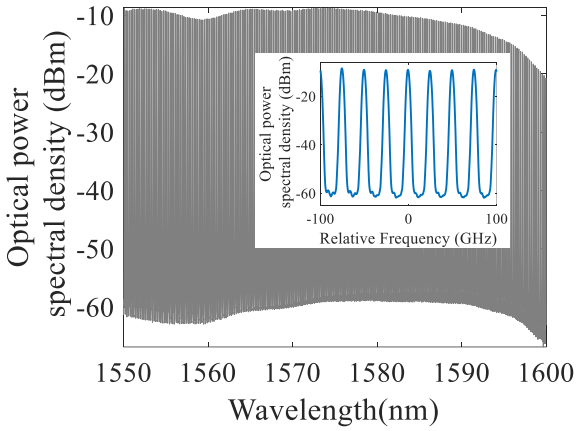

Figure 3. 3 Power spectral density of the 25 GHz-pitched optical parametric comb. The local zoom of the spectrum over frequencies relative to seed laser frequency in the inset shows the 25 GHz spacing of the comb lines.

To synthesize the sub-GHz flat-top filter, 221 comb lines of this spectrum were selected. The sought-after amplitude and magnitude of the applied filter coefficients in the time domain are

shown in Figure 3.4. Relating to the experimental schematic shown in Figure 3.2, the attenuation in pulse shaper #1 was programmed based on the magnitude of these coefficients. The pulse shapers in the setup were commercial device Waveshaper 4000XS covering both C and L bands. Following the amplitude shaping an EDFA was inserted in the setup to make up for the losses and ensure optimal signal level management.

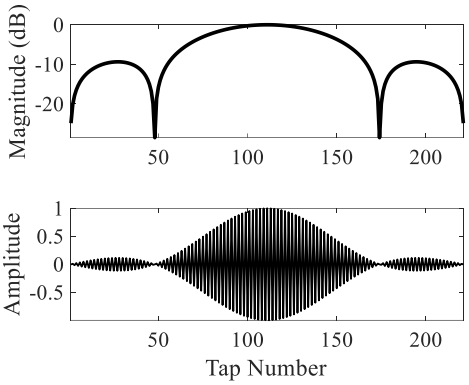

Figure 3. 4 Normalized magnitude and amplitude of the sub-GHz flat-top filter coefficients in the time domain.

The 45 nm bandwidth of the optical spectrum selected for the 221 taps (comb lines) filter implementation covers a portion of both C and L bands. Therefore, the EDFA in the setup was specifically designed to have its gain spectrum centered at 1565 nm. A 10:90 coupler was used after the EDFA, where 90 percent of the input power was directed toward the lower arm of the interferometer due to higher optical loss in this arm. The modulator used in the experiment had a half-wave voltage (i.e., the V_π) of 8.1 V.

In the experiment, the dispersive medium used to impose the appropriate delay between the tap coefficients consisted of a span of DCF with a measured dispersion of -81.92 ps/nm at 1545 nm and a total length of only 0.6 km – in sharp contrast to the previous implementations which

universally used long fiber lengths for the same purpose. The group delay of the fiber was measured over the 1550-1600 nm wavelength range and is shown in Figure 3.5. Ideally, in the setup under consideration, the dispersive medium ought to introduce a quadratic phase only - to closely replicate the designed FIR RF-photonic filter. However, as the variation of the second derivative of group delay in Figure 3.5 implies, up to fourth-order dispersion of the DCF should be considered in our experiment. In fact, $\theta_3 = -0.75$ (ps^3) and $\theta_4 = 0.0085$ (ps^4) at 1574.9 nm wavelength are obtained by polynomial fitting of measured total group delay of the DCF and considering that $\tau = \frac{d}{d\omega}\beta$.

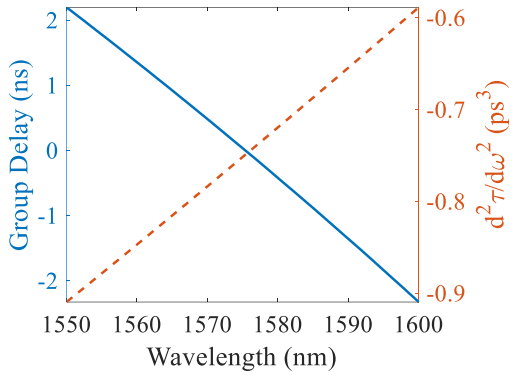

Figure 3. 5 (solid line) Measured group delay of the DCF over 1550-1600 nm, (dashed line) Second derivative of group delay which its variation implies presence of nonzero fourth-order dispersion of the DCF. Polynomial fitting of measured group delay shows that $\theta_3 = -0.75$ (ps^3) and $\theta_4 = 0.0085$ (ps^4) at 1574.9 nm wavelength.

The optical signal at the output of the DCF was detected using a photodiode with a 3dB bandwidth of 20 GHz.

To rigorously capture the filter shape and quality, the modulator was driven by two different sets of RF waveforms. First, a vector network analyzer was used to generate a frequency sweep and characterize the filter transfer function. Wherein, the maximum input RF voltage of 0.79 V was used to satisfy the small-signal assumption made in section 3.2. Once the desired filter

response was achieved by programming the intra-interferometer pulse shaper, an RF digital signal generated by an Arbitrary Waveform Generator (AWG) was used as a test signal. The output RF signal was detected by a digital sampling oscilloscope and the data was demodulated and analyzed offline.

We next proceed to the presentation of the experimental results.

3.4.Experimental Results

3.4.1. Filter response

As already specified in the previous section, the optical parametric comb with spectrum shown in Figure 3.3 served as the multi-wavelength source in the narrow flat-top filter realization. The magnitude of the filter time-domain coefficients imposed by pulse shaper #1 is shown in Figure 3.4. The shaped optical spectrum measured after the DCF, with the modulator arm disconnected, is shown in Figure 3. 6.

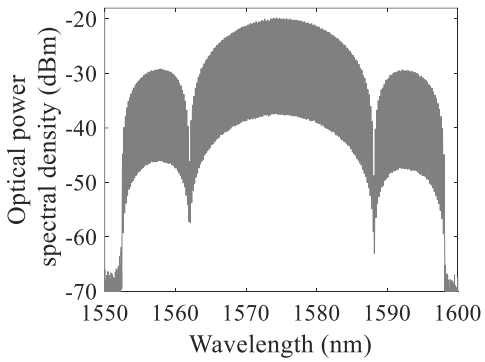

Figure 3. 6 Shaped optical power spectrum including 221 comb lines measured at the output of DCF. This pulse-shaper configuration was used for all experimental measurements.

Figure 3.7 shows the resulting filter spectral shape when the intra-interferometer pulse shaper phase was programmed based on the time-domain coefficients shown in Figure 3.4, in the absence of any dispersion compensation. As expected, the unwanted higher-order dispersion causes severe distortion in the spectral shape of the pre-designed narrow flat-top filter. This broadened asymmetric spectrum is not caused by TOD only, however. As stated previously, the 45 nm bandwidth of the comb is sufficiently large to be affected by both third and fourth-order dispersion. To explicitly demonstrate the last claim, the filter transfer function was simulated considering only β_2 and β_4 of the DCF. The simulation results are shown in Figure 3.7. As is apparent in Figure 3.7, the filter response is still distorted even without any TOD. Specifically, the fourth-order dispersion of the DCF results in asymmetry and ringing on one side of the filter spectral shape.

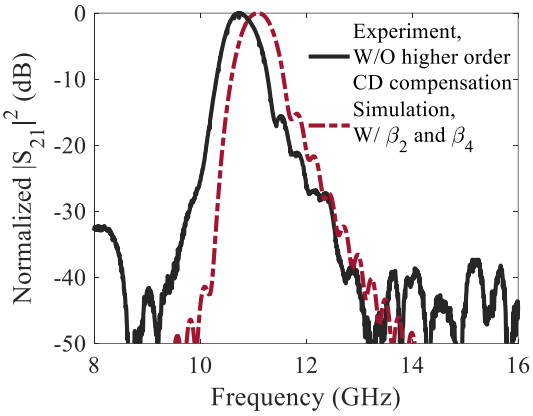

Figure 3. 7 (solid line) Measured filter transfer function without any higher-order Chromatic Dispersion (CD) compensation, (dashed line) Simulated filter transfer function considering only β_2 and β_4 of the DCF.

Next, the pulse shaper in the interferometer was programmed according to Eq. 3.8 to correct the tap delay from its departure caused by the higher-order dispersion. Like amplitude programming in pulse shaper #1, the phase programming of pulse shaper #2 is done iteratively due

to the limited accuracy of the pulse shapers and the optical network analyzer device used for measuring the group delay of the DCF. As shown in Figure 3.8, a narrow – 715 MHz-wide flat-top filter was indeed obtained upon full higher-order dispersion compensation, showing an excellent agreement with the original filter design. In particular, we note that this demonstration represents the first flat-top comb-based sub-GHz RF-photonic filter. It equally ought to be emphasized that the high-OSNR wideband comb generation, as well as the compensation of the fourth-order dispersion, applied for the first time, to the best of our knowledge, in RF-photonic filter shaping, were the critical steps in the successful filter realization.

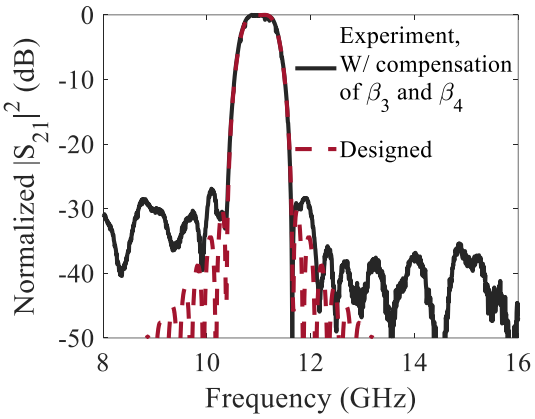

Figure 3. 8 (solid line) Measured filter transfer function with higher-order dispersion compensation, (dashed line) Designed filter transfer function.

It is likewise important to note that only a 0.6 km-long DCF piece was used in the implementation in contrast to the previous demonstrations for flat-top filters with 3 dB bandwidths of few GHz [33], [50], which invariably relied on significantly longer fibers. The utilization of a short waveguide in our setup also resulted in a large Free Spectral Range (FSR) of 53 GHz for the filter. Therefore, the unwanted higher frequency image passband, expected from a double-sideband modulation in our scheme, was sufficiently far away from the main passband.

Consequently, the obtained filter could be regarded as a single-passband variety in the considered frequency range, for all intents and purposes, which significantly simplified the implementation. Namely, the large FSR is also considerably beneficial in the compensation of higher-order dispersion in double-passband filters. According to Eqs. 3.9 and 3.10, the higher-order dispersion necessarily imposes different unwanted phase distortions for the lower and upper passbands. The latter effect necessarily leads to an asymmetric broadening of one of the filter bands, which can result in the overlap between the filter images. We note that the effect has been rendered inconsequential in our implementation with a (relatively) short waveguide.

In addition to the above, we note that the utilization of a short piece of DCF in the filter realization straight-forwardly translates to a lower filter latency, compared to implementations using kilometer lengths dispersive fiber [51].

3.4.2. Filter Central Frequency Tuning

The constructed narrowband RF-photonic filter was also freely tunable. The center frequency of the filter was shifted by varying the optical delay in the upper arm of the interferometer. The captured spectra at five different center frequencies of 11, 11.75, 13.17, 13.75, and 14.43 GHz, shown in Figure 3. 9, illustrate the shape-invariant tunability throughout the tuning range.

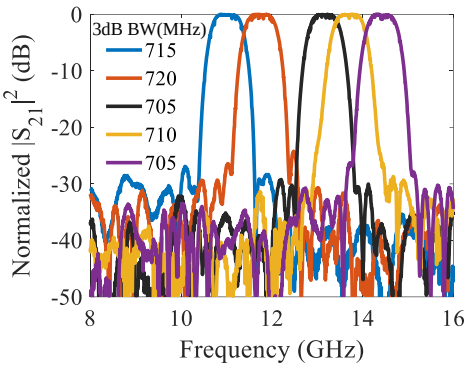

Figure 3. 9 Measured filter transfer function when filter center frequency was tuned by varying the optical delay in the interferometer and higher-order dispersion of the DCF was compensated (3dB bandwidth (MHz) of each filter is mentioned in the figure).

Figure 3.10 shows the corresponding filter response when no higher-order dispersion compensation was carried out. By varying the optical delay in the upper arm of the interferometer from 94 ps to 96.5 ps, the center frequency of the filter was shifted from 10.74 GHz to 14.16 GHz. As expected, a further severe distortion of filter spectral shape is observed with the filter central frequency tuning (see Figure 3.10).

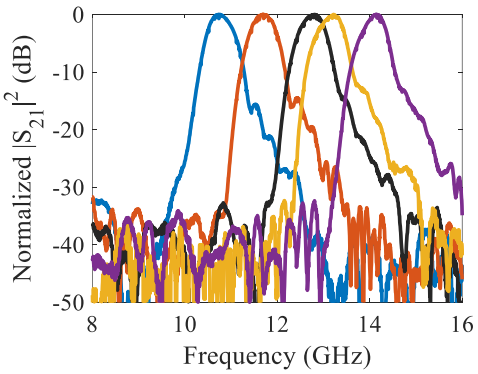

Figure 3. 10 Frequency tuning the filter from 10.74 GHz to 14.16 GHz by varying the optical delay in the upper arm of interferometer from 94 ps to 96.5 ps (without any compensation of higher-order dispersion of the DCF).

3.4.3. RF Digital Signal Filtering by the RF-Photonic Filter

In addition to the VNA-based characterization, we tested the filter effectiveness on a set of RF signals with different modulation formats and bandwidths. In these experiments, we have emulated an analog RF transceiver [56]. The RF digital modulated signal generated by an AWG was imposed to the MZM and the RF output signal was detected by a digital sampling oscilloscope. The captured data was demodulated and analyzed offline. In effect, the data retrieval emulated an ideal analog RF transceiver without any attempt to compensate, or otherwise mitigate the nonlinear characteristic of the electro-optic modulator and the photodetector. The measurement was repeated at three different filter center frequencies with which the input RF signal carrier frequency was aligned. The constellation diagrams and QF of the retrieved data with carrier frequencies of 11, 13.17, and 14.43 GHz are shown in Figures. 3.11-3.13. We note that the QF in all the measurements represents the worst-case closest neighbor pair-wise constellation points' performance for a given modulation case.

As shown in Figure. 3.11, 400 and 700MBaud QPSK data with the carrier frequency of 11GHz were successfully retrieved with a QF of 23dB. On the other hand, the QF for the 900MBaud QPSK case was reduced to 19.1 and 18.3 dB for carrier frequencies of 13.17 and 14.43 GHz, respectively, due to filtering. The 400MBaud 16-QAM signal with a carrier frequency of 11, 13.17, and 14.43 GHz, were also well recovered with QF's of 12.9, 11.9, and 10.8 dB, as shown in Figures. 3.11-3.13.

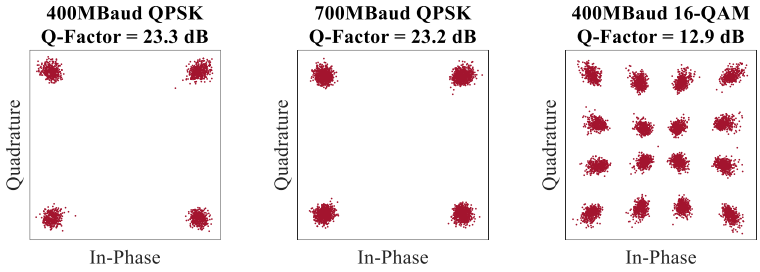

Figure 3. 11 Constellation of filtered RF channels with the carrier frequency of 11 GHz and different modulation formats and bandwidths. The center frequency of the filter was aligned to the carrier frequency of the input RF channel.

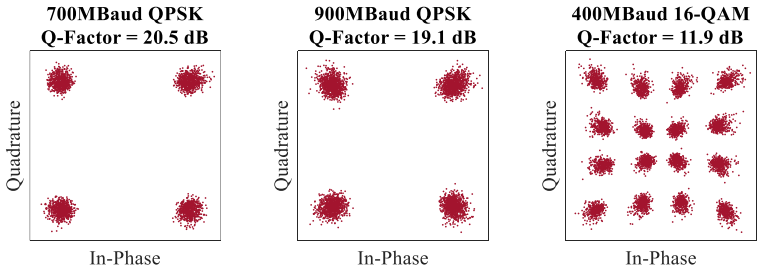

Figure 3. 12 Constellation of filtered RF channels with the carrier frequency of 13.17 GHz and different modulation formats and bandwidths. The center frequency of the filter was aligned to the carrier frequency of the input RF channel.

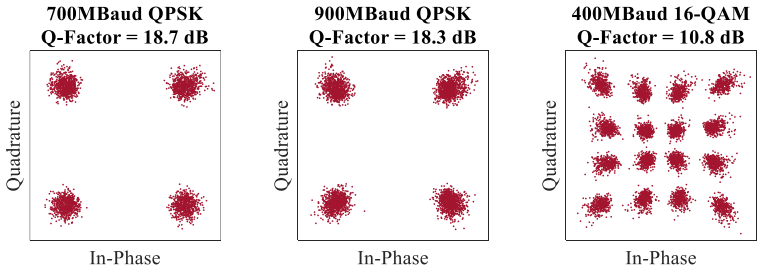

Figure 3. 13 Constellation of filtered RF channels with the carrier frequency of 14.43 GHz and different modulation formats and bandwidths. The center frequency of the filter was aligned to the carrier frequency of the input RF channel.

The decay in the QF with the carrier (and filter central frequency) tuning is attributed to the frequency response of the RF photonic link, and the modulator characteristic, in particular. This link characteristic had to be and has been compensated in the experiment. The link frequency response was measured when the DCF was removed from the setup, as shown in Figure 3.14. We note that in order to compare the measurement results with the simulations in the previous section, this frequency response was de-embedded from the measurement setup as explained in [41]. In particular, the de-embedding was used in results shown in Figures. 3.7-3.10.

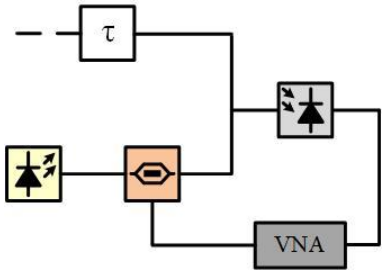

Figure 3. 14 The experimental setup to measure the frequency response of the RF photonic link.

The obtained frequency response of the link shown in Figure 3.14, clearly demonstrates a roll-off causing the performance deterioration with the increased carrier frequency mentioned in the previous paragraph.

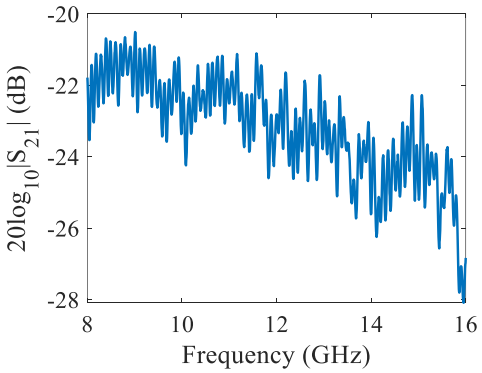

Figure 3. 15 The link frequency response without DCF.

After the successful demonstration of the filtered reception of a single RF channel with different modulation formats and speeds, the full filter bandwidth was loaded with seven 100MBaud RF channels having the center frequency spacing of 104 MHz at the center frequency of 11 GHz, thus emulating a 7-channel sub-carrier transmission scenario in a small cell 5G-like configuration, albeit at a center frequency not necessarily compliant with that standard [53]. Nevertheless, the central frequency of the experiment in no way diminishes the quality of the obtained results. Two different channel loading conditions were tested. At first, all channels were 16-QAM modulated. In the second experiment, the two outmost channels were QPSK modulated with the rest still maintained at 16-QAM modulation, emulating an adaptive bandwidth water-filling scenario. In offline analyzing the retrieved RF data, each channel was filtered out and the QF of each one was calculated, separately. QFs of the demodulated data for the two scenarios are shown in Figures. 3.16 and 3.17 and attest to the successful retrieval of the data and an excellent filter shape integrity for the relevant RF applications.

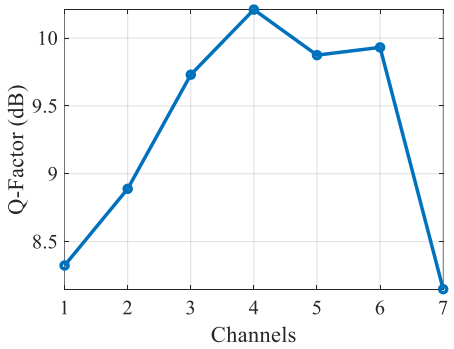

Figure 3. 16 Q-Factor of filtered reception of seven 100MBaud 16-QAM RF channels with 104 MHz center frequency spacing. In post-processing of captured RF data, each channel was filtered out and its Q-Factor was calculated.

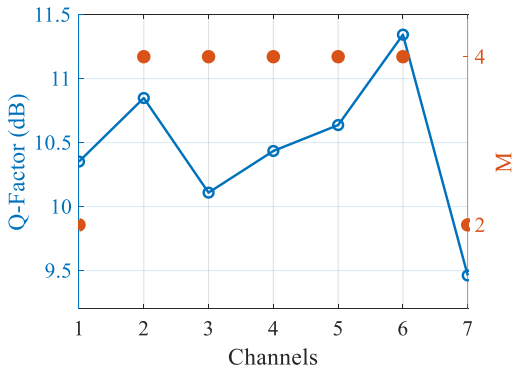

Figure 3. 17 Q-Factor of filtered reception of seven 100 MBaud RF channels with 104 MHz center frequency spacing. In post-processing of captured RF data, each channel was filtered out and its Q-Factor was calculated (In the Figure, M= 4 indicates 16-QAM modulation and M =2 refers to QPSK modulation).

The digital modulation performance characterization presented serves as to attest the implemented filter integrity, short of the full extent digital signal characterization in terms of the bit-error-rate curves, which – in view of the number of the cases and scenarios considered would likely be distracting from the main contribution of this work.

3.5.Summary

We have synthesized the first sub-GHz flat-top RF-photonic filter using a wide bandwidth all-fiber parametric frequency comb. The measured 715 MHz-wide filter had a high-quality flat-top spectral profile and its shape-invariant tunability was also demonstrated. The new filter construction was enabled by a high accuracy third and fourth-order dispersion compensation adaptively applied to each comb line using a pulse shaper. In addition to the filter characterization by a VNA, its integrity was also verified on RF digital signals. Specifically, a successful single RF channel retrieval at three different carrier frequencies for QPSK and 16-QAM modulation with symbol rates ranging from 400 to 900MBaud was demonstrated. Additionally, up to seven

100MBaud subchannels with 104 MHz spacing fully occupying the filter bandwidth and carrying QPSK and 16-QAM modulation were also successfully retrieved (as demonstrated by the performance shown in Figures. 3.16 and 3.17), fully attesting the realized filter compliance with the RF signals of high practical interest.

The new narrow bandwidth filter synthesis paves the way for tunable bandpass RF filtering at remote 5G nodes; relaxing the high-resolution requirement on the necessary ADCs, whereas a number of novel concepts introduced in this work enable previously unattainable performance, which open a door to new applications and architectures in the field of RF photonics.

Chapter 3, in part, is a reprint of the material as it appears in Journal of Lightwave Technology, vol. 38, no. 6, pp. 1194–1201, (2020), titled "Demonstration of a Sub-GHz Flat-Top Comb-Based RF-Photonic Filter Enabled by Fourth-Order Dispersion Compensation" by Zahra Serahati, Eduardo Temprana, Evgeny Myslivets, Vahid Ataie, Nikola Alic, and Stojan Radic. In addition, Chapter 3, in part, is a reprint of the material as it appears in 2019 IEEE Photonics Conference (IPC), 2019, pp. 1–2, titled "Demonstration of the First Sub-GHz Comb-based RF-Photonic Flat-top Filter" by Zahra Serahati, Eduardo Temprana, Evgeny Myslivets, Vahid Ataie, Nikola Alic, and Stojan Radic. Lastely, Chapter 3, in part, is a reprint of the material as it appears in Frontiers in Optics 2019, paper FTu5B.5., titled "Compensation of Fourth-Order Dispersion Induced Distortion in Comb-Based Microwave Photonic Filters" by Zahra Serahati, Eduardo Temprana, Evgeny Myslivets, Vahid Ataie, Nikola Alic, and Stojan Radic. The dissertation author was the primary investigator and the primary author of these articles.

Chapter 4 Chromatic Dispersion Compensation in Parametric Channelizer Assisted High-Baud Rate Coherent Receiver

4.1.Introduction

We shall now depart from the analog applications and will shift the attention to arguably the most salient utility of photonics – namely high-speed fiber optic communications. Considering the constant growth rate of the global internet capacity of approximately 30% per year [57], as we said before, there exists a definite necessity for higher speed, and more cost-effective optical communication network infrastructure [58]. With this ever-increasing demand driven by 5G applications, cloud computing, high-definition videos, and artificial intelligence, it should come as no surprise that the global Internet Protocol (IP) traffic is expected to reach 4.8 ZB (10^{21} bytes) as soon as 2022 [58].

Historically, the system capacity increase has been enabled by the momentous evolution of optical transmission systems. During the 1990s, the emergence of practical Erbium-Doped Amplifiers (EDFAs), which provided a large gain over a wide bandwidth, laid the foundation to the establishment of wavelength-division multiplexed intensity-modulation and direct-detection (WDM-IMDD) systems [59]. However, the intensity-only modulation in these systems restricted the increase of system capacity within the so-called Conventional band (C-band) portion of the infrared spectrum. Soon after, the commercialization of coherent optical communication systems has offered a significantly higher spectral efficiency with respect to the systems from the 20^{th} century. In fact, optical coherent intradyne detection was indeed the breakthrough technology for achieving 100Gb/s per wavelength channel [58]. Single-carrier 400 Gb/s bit rate with the total system capacity of 20 Tb/s, or more, have been established in the contemporary commercial WDM systems. Furthermore, single-carrier data transmission with more than 1 Tb/s has been

implemented in the laboratory, whereas the next generation 800 GbE or even 1.6 TbE (10^{12} bits Ethernet) are also on the horizon [3], [59], [60].

As noted previously, in coherent optical systems, information is encoded in the amplitude, phase, and polarization of light. And with the relatively high receiver sensitivity, optical coherent communication systems support data transmission at higher speed and extended reach on each of its numerous wavelength channels [59]. Besides that, access to the full electric field information allows mitigation of the transmission impairments using digital signal processing.

To increase the data rate transmitted by a single-wavelength (or equivalently – a carrier) coherent optical system, one can generate either higher-order QAM formats or increase the baud rate. The former requires a higher OSNR for detection and is less tolerant to the phase noise and nonlinear effect. Also, very high order QAMs are difficult to generate and detect owing to the associated reliance on high-resolution digitizers [3]. In fact, as a general rule, the Effective Number of Bits (ENOB) is a monotonically descending function with bandwidth [61]. Therefore, increasing the signal baud rate is a more promising candidate to increase the system capacity. Indeed, the growth trend of the baud rates for different QAM orders indicates its increase with a pace of 12 GBd per year [3]. Presently, the highest generated (square root) raised cosine-shaped QAM modulations have been: the 220 GBd QPSK [1] and 128 GBd 16-QAM [2].

Nevertheless, high baud rate transmission has challenges of its own. Firstly, the high baud-rate signal becomes more susceptible to Chromatic Dispersion and Polarization Mode Dispersion. Considering that the chromatic dispersion penalty is proportional to $\propto R^2 L$ [62], where R is the symbol rate and L is the transmission length. In fact, the CD compensation is one of the most power-hungry blocks of the DSP chain in high baud rate or/and long-haul transmission [63], [64].

More importantly, wide-bandwidth (i.e., high speed) optoelectronic components, e.g., photodetector, trans-impedance amplifier, ADC, and electronic processors or Application-Specific Integrated Circuits (ASICs) are needed in high-baud rate transmission systems. In the demonstrations of high-baud rate transmission so far, the bandwidth limitation of the optical and electrical components has usually been mitigated by taking advantage of digital equalizers [1], [57].

The low bandwidth and sampling speed of the commercially available (digital) converters, e.g., ADCs, is a dominating barrier toward high-baud rate transmission [65]. As mentioned before, one of the main advantages of coherent optical communication is the ability to digitally mitigate transmission impairments. And digitizers are the essential components enabling digital signal processing.

It should be noted that the precision of the high-speed ADCs is limited at high data rates [66]. Moreover, the integration of ADCs with the digital signal processor, requires that the former be implemented in Complementary metal-oxide-semiconductor (CMOS). However, the fastest CMOS converters still have relatively speaking – moderate electrical bandwidths, e.g., BW $\propto$ 20 GHz for 92 GS/s ADC [65], [67]. While InP-based converters have provided real-time oscilloscopes with beyond 200 GS/s sampling rate and bandwidths beyond 100 GHz, they cannot be utilized in commercial communication systems due to their inherent incompatibility with the CMOS process, high cost, and high power consumption [67]. As a more practical solution, high-speed converters with sampling rates higher than 100 GS/s and up to 60 GHz BW have been proposed in Si/SiGe Fully Depleted Silicon on Insulator (FDSOI) CMOS and SiGe Heterojunction Bipolar Transistor (HBT) Bipolar CMOS (BiCMOS), which could be placed in-between the trans-impedance amplifier and CMOS ASIC [67], [68]. In [69], the reception of optical 2×56-GBaud

QPSK signal was reported by electrical spectrum decomposition technique using ultra-broadband electrical bandwidth divider. However, even in these configurations, high-speed photodetector and TIA were needed.

In [70], the reception of 214 GBd PDM-QPSK was demonstrated using a 228-GHz spectrally sliced coherent receiver, wherein the wide bandwidth of the optical signal was divided into six narrower frequency bins by an optical demultiplexer, and comb lines of an optical frequency comb were used as a local oscillator for coherent detection. However, as the importance of dual-comb configuration for channelization is clarified in [71], the requirement of precise optical signal-filter alignment and flattop filter response limits the application of the spectrally sliced receiver reported in [70].

Considering these restrictions, our study has focused on the architecture entailing hybrid optical and electrical signal processing enabling high-quality CD mitigation of high-baud rate single-carrier optical signals. Based on simulations, we have accomplished 214GBd QPSK and 107GBd 16-QAM, high-quality CD compensation of the wideband signals based on a parametric optical channelizer. The physically assisted CD compensation relied on commercially available low-speed optoelectronic components, analog-to-digital converters, and filter-bank-based DSP. The results presented are based on a rigorous simulation developed in a close match with the extensive experimental results on parametric amplification, multicasting, and channelization [16], [71]–[75].

The remaining part of this chapter is organized as follows. In section 4.2, the principle of parametric optical channelizer is described, including the details of the designed 8-channel construct, which was used for processing. Also, the principles of the developed sub-band digital

CD compensation and signal reconstruction are explained. The results are summarized in section 4.3, whereas the overview of the work and its implications are contained in section 4.4.

4.2.Physically assisted chromatic dispersion compensation using an optical channelizer

The optically assisted processing architecture based on a parametric optical channelizer is shown in Figure 4.1. Stemming from the general concept of the parametric channelizer [72], the fundamental proposition of the architecture shown in Figure 4.1 is to divide the wide bandwidth of the incoming high-baud rate optical signal into a number of narrower frequency bins and coherently detect each of them. The received (and converted) photo-detected signal is then sent to a set of high-resolution and low-speed Analog-to-Digital Converters. After the 'per sub-channel' mitigation of chromatic dispersion, a digital filter bank is utilized to reconstruct the wideband signal from the channelized slices.

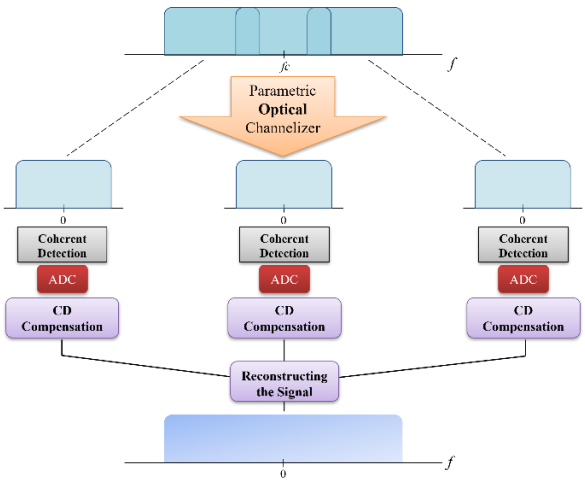

Figure 4. 1 Physically assisted chromatic dispersion compensation using an optical channelizer.

4.2.1. Principle of Parametric Optical Channelizer

The received high-baud rate optical signal is first replicated on a Δf-pitched frequency grid by a parametric mixer, which is described in detail in [73]. For the sake of general description, for the time being, let us suppose that the parametric multicasting is ideal, i.e., each copy is an exact replica of the received signal. Then, a frequency locked comb with $\Delta f + \delta$ spacing and precisely offset from the multicast grid is used as a bank of local oscillators, as shown in Figure 4.2a. Each tone of this reference comb is mixed with the closest signal replica in a separate coherent receiver and the low-pass frequency response of the photodiode acts as an electrical filter, shown in Figure 4.2b. The coherently detected signal of each sub-channel (i.e., a slice) is digitized, and the full-field analysis and processing are performed in the digital domain on a per-sub-channel' basis.

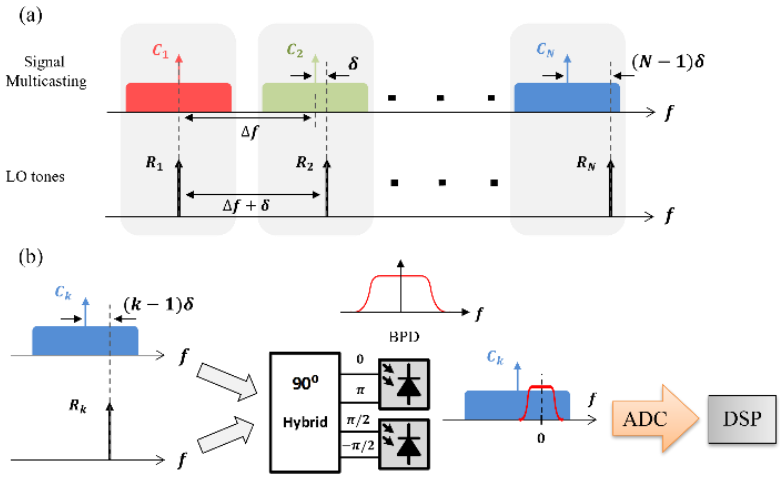

Figure 4. 2 Principle of Parametric Optical Channelizer. a) Multicasting comb and corresponding LO tones. b) coherent detection of each pair of signal copies and the corresponding LO tone.

Nevertheless, in a parametric multicasting mixer, the generated new sidebands through Modulation Instability (MI) and phase conjugation are phase-conjugates of the original signal [74], i.e., $x_{new}(t) = x^*(t)$. Thus, phase conjugation in the frequency domain implies spectral reversal: $X_{new}(\omega) = X^*(-\omega)$ [76], whereas, the phase-conjugated copies in our designed 8-channel optical channelizer ought to be sampled at $\omega = \omega_c - n\delta/2$ instead of $\omega = \omega_c + n\delta/2$, where ω_c is the

center frequency of the copy and δ is the channel spacing. Therefore, the required frequency sampling of the channelized spectrum cannot be accomplished by a single equispaced LO comb. Instead, two LO combs with a frequency pitch of $2\Delta f_M + 2\delta$ and $2\Delta f_M - 2\delta$ are needed to accomplish the proper sampling in frequency. Alternatively, every other copy could be used for channelization, avoiding the conjugate copies (i.e., with a multicasting comb with frequency spacing of $2\Delta f_M$). However, the latter approach would result in the doubling of the comb spectral span requirement.

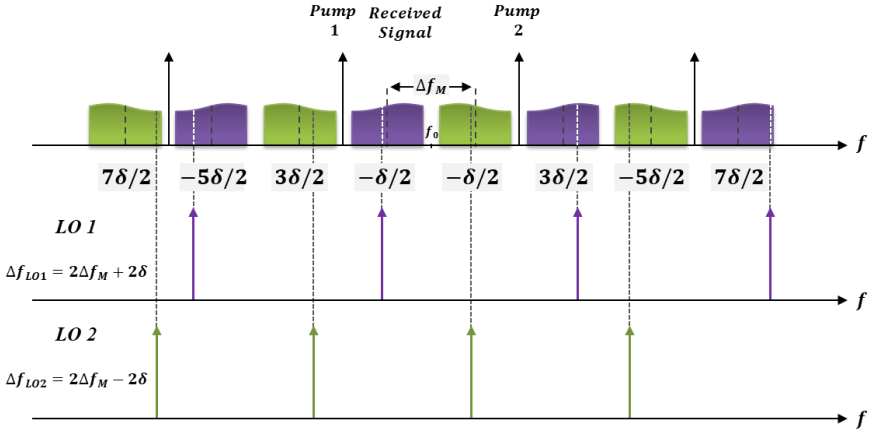

Figure 4. 3 Sampling the multicasting comb with two LO combs with a frequency pitch of $2\Delta f_M + 2\delta$ and $2\Delta f_M - 2\delta$.

The parametric mixer design for multicasting and both LO combs was the same as discussed in [16]. These dual pump mixers, as shown in Figure 4.4, consist of a cascade of compression stage and mixer, which is a Dispersion-Flattened Highly Nonlinear Fiber (DF-HNLF). The compression stage itself was a cascade of high-γ HNLF and SMF, where γ is the nonlinear coefficient of the fiber. As mentioned in Figure 4.4, the positive chirp introduced by the highly nonlinear fiber followed by the positive dispersion in SMF results in pulse compression and the generation of high peak power pulses. Mixer Figure of Merit (FoM) is proportional to $\propto \gamma P_{Peak} L$,

where the P_{Peak} is the peak power of the incoming pulses and L is the length of the mixer. Thus, as mentioned in section 3.3, the generation of high peak power shock waves in the compression stage increases the efficiency of mixing and results in the generation of a higher number of frequency tones.

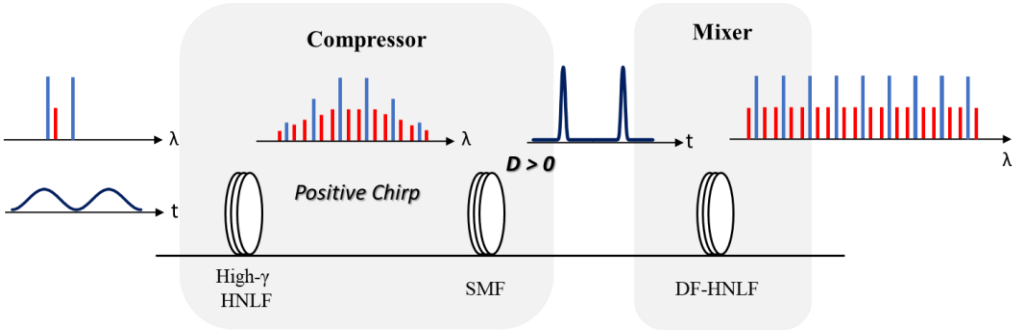

Figure 4. 4 Parametric mixer consisting of a cascade of compression stage and mixer.

An 8-channel parametric channelizer with channel spacing of 29.47 GHz was designed as follows: The frequencies of the pump lasers for multicasting comb were 193.04 THz and 194.51 THz; conversely, the pump frequencies for the LO1 comb (i.e., that sampling even channels as shown in Figure 4. 3) were 193.4 THz and 194.16 THz, whereas those for the LO2 (sampling the odd channels) the pump lasers frequencies were 193.42 THz and 194.13 THz. The pump lasers of our dual-pump parametric mixers were followed by an EDFA with a Noise Figure (NF) of 6dB and output power of 32dBm. The carrier frequency of the QAM signal was 193.41 THz. The High-γ HNLF had a nonlinear coefficient of 18.46 W/km, dispersion parameters of D = -0.5 p$s/nm/km$ and dispersion slope = 0.03 $ps/nm^2/km$, and for the SMF the dispersion parameters were D = 17 p$s/nm/km$ and dispersion slope = 0.06 $ps/nm^2/km$. The DF-HNLF fiber had a nonlinear coefficient γ of 8.46 W/km and a dispersion profile as shown in Figure 4. 5.

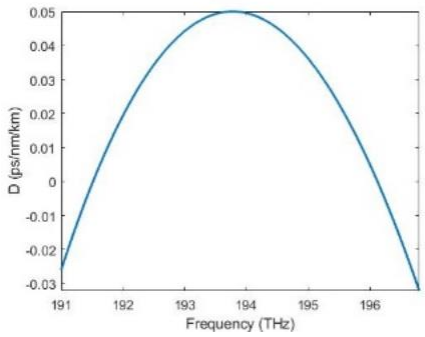

Figure 4. 5 Dispersion profile of the DF-HNLF.

The lengths of high-ɣ HNLF, SMF, and DF-HNLF in the multicasting comb were 12m, 0.8m, 50m, respectively; while in the LO1 they corresponded to 15m, 2.3m, and 40m, and in LO2 amounted to 15m, 2.7m, 40m. The resulting parametric channelizer spectrum is shown in Figure 4. 5. It covers 5.4 THz (43.11 nm). The channelizer was optimized with respect to the crosstalk and not necessarily for the noise figure.

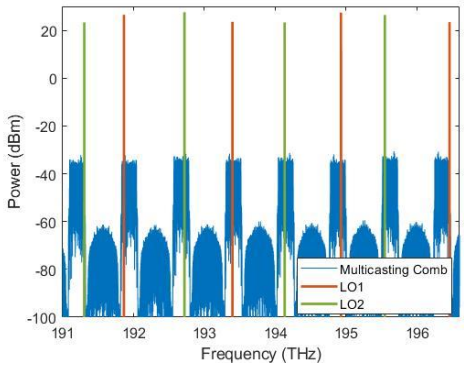

Figure 4. 6 Parametric channelizer spectrum: Multicasting comb and LO tones.

However, in reality, the parametric response is not uniform across the generated signal replicas, as supposed at the beginning of the sub-section 4.2.1. The last fact is easily recognized in Figure 4. 6, wherein power variation across replicas is clearly observed. Another aspect that requires attention in processing is the finite and varying dispersion of the fibers in the setup, which introduces a varying phase response, as well as unequal delays across the replicas. Therefore,

signal slices need to be equalized prior to processing and signal reconstruction. Specifically, in order to align the detected signals in each channel and reconstruct the signal perfectly, this power and phase variation were equalized prior to the standard digital signal processing. The complex transfer function of the bands' equalizer was extracted from the system response to a known training signal sequence at back-to-back, for averaged multiple (noise) realizations.

4.2.2. Sub-band Chromatic Dispersion Compensation and Signal Reconstruction

As is well known, coherent detection allows for straightforward chromatic dispersion mitigation by DSP. In contrast, to the most pursued compensation in the Fourier domain over the whole spectrum, here the CD compensation is performed on each extracted sub-band, prior to signal reconstruction.

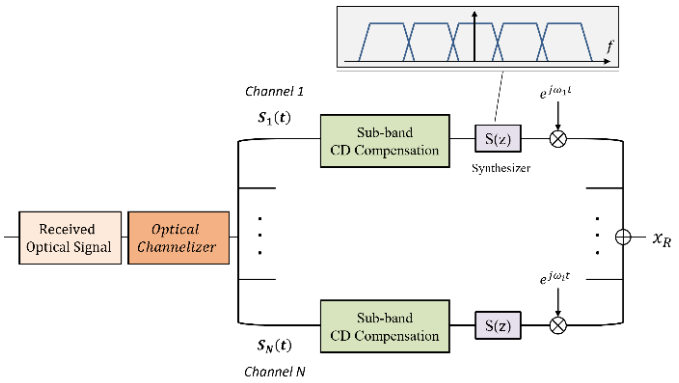

Figure 4. 7 Digital signal processing of the detected signal in each channel.

A bank of trapezoid filters [77] was used for perfect signal reconstruction, as shown in Figures 4. 7. and 8.

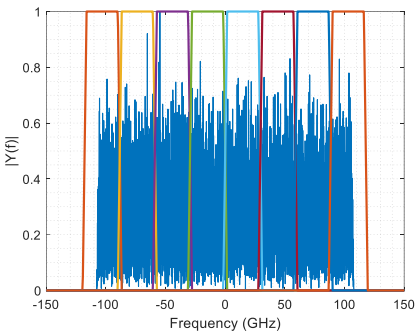

Figure 4. 8 Bank of trapezoid filters over the whole spectrum of the high-baud rate signal.

The transfer function of chromatic dispersion (in the frequency domain) can be expressed as follows:

$$H_{CD}(\omega) = e^{jK\omega^2}, K = \frac{DL}{4\pi C_0}\lambda_0^2,$$

where D is the dispersion coefficient of the fiber, L is the propagation length, λ_0 is the wavelength of the carrier and C_0 is the speed of light.

If we divide this frequency range of $\omega \in \Omega$ into narrower frequency bins $\omega \in \Omega_0$, chromatic dispersion compensating filter in each bin becomes:

$$H(\omega + \omega_i) = e^{-jK(\omega+\omega_i)^2} =$$

$$e^{-jK{\omega_i}^2} e^{-j2K\omega_i\omega} H_{sub}(\omega)$$

where ω_i is the center frequency of each bin and $H_{sub}(\omega)$ is common among all sub-bands:

$$H_{sub}(\omega) = e^{-jK\omega^2}, \omega \in \Omega_0.$$

The transfer function of the chromatic dispersion for the signal over frequency range $\omega \in \Omega$ has a form of an all-pass filter [19].

4.3.Results

The results presented in this section were obtained by VPIphotonics software rigorously replicating the systems and sub-systems of the single polarization channelizer architecture experiments performed by the Photonics Systems Group. In all transmission simulations, the spans of 75km SMF, with D = 17 ps/nm/km and 0.2 dB/km attenuation, cascaded by an EDFA with NF of 6dB were used in the transmission link. The transmitted signal pulses had raised cosine shape with a roll-off factor $\beta = 0.01$. Since lasers with finite linewidths were used in all simulations, the Carrier Phase Estimation (CPE) was performed in the DSP chain.

In Figure 4. 9, shown are the back-to-back constellation diagrams of 214GBd QPSK as well after transmission over L = 75km fiber and CD compensation without analog to digital discretization. In these simulations, the laser linewidth of the signal carrier and LO for the full-bandwidth detection were 102 kHz and the linewidth of the pump lasers in all three combs was 25.5 kHz. The QF of the back-to-back optical transmission of 214GBd QPSK is 22.69dB. The QF of signal detection using optical channelizer, after CD compensation and CPE, was reduced to 17.08dB, owing to the noise added by the EDFAs (with NF = 6 dB) in the transmission link, as well as the parametric channelizer.

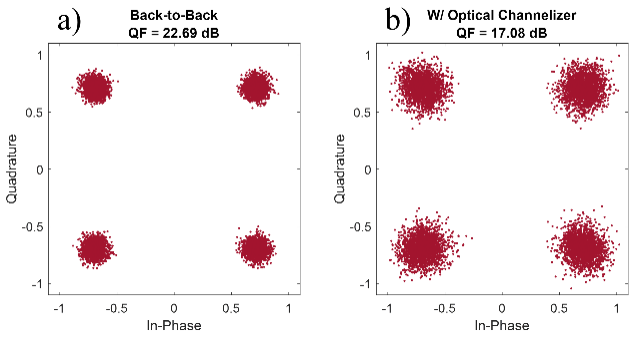

Figure 4. 9 Constellation of 214GBd QPSK: a) Back-to-Back. b) After transmission (L = 75 km) and CD compensation using Optical Channelizer without analog-to-digital conversion.

The QF evolution with the propagation distance for 214GBd QPSK signal and CD compensation relying on the optical channelizer is shown in Figure 4. 10. The results show a maximum transmission reach of about 600km. The assumed threshold QF for the maximum reach was 10dB considering the 7% FEC overhead assumed in the transmission [78].

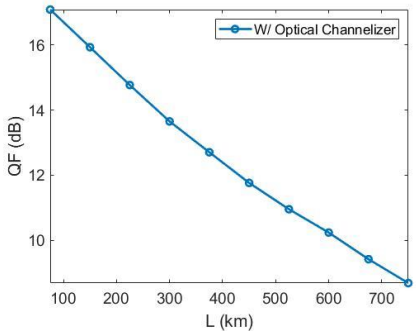

Figure 4. 10 QF versus transmission length in 214GBd QPSK transmission with CD compensation using the optical channelizer (signal and LO laser linewidth is 102 kHz, and the pump laser linewidth is 25.5 kHz), without analog-to-digital conversion.

The performance of CD compensated 107GBd 16-QAM was also studied. In this case, only four sub-channels were sufficient for the signal channelization, with the filter-bank channel spacing maintained at 29.47 GHz. The QF of back-to-back detection, as shown in Figure 4. 10, is 17.56dB. The CD compensation based on the optical channelizer after 75km transmission yielded a QF of 13.57dB.

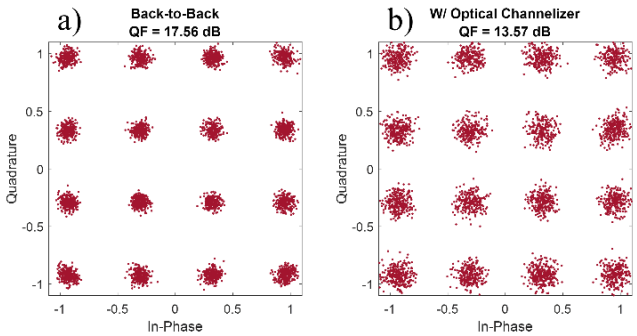

Figure 4. 11 Constellation of 107GBd 16-QAM: a) Back-to-Back. b) After transmission (L = 75 km) and CD compensation using Optical Channelizer without A-to-D discretization.

As inferred by the QF trend shown in Figure 4. 11 for different transmission lengths, 107GBd 16-QAM, the maximum transmission length enabled by the parametric channelizer corresponds to over 400km.

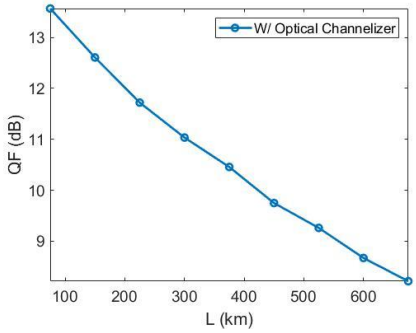

Figure 4. 12 QF versus transmission length in 107GBd 16-QAM transmission with CD compensation using the optical channelizer (All lasers' linewidth is 25.5 kHz)., without analog-to-digital conversion

In all the results discussed so far, signal processing has been done on the continuous amplitude detected electrical signals. However, the critical component defining the overall system performance in high-speed systems is the analog to digital converter. Therefore, the main advantage of the channelized approach is the ability to rely on a number of relatively small bandwidth and high-resolution ADCs (as opposed to a single digitizer covering the full bandwidth of the signal yet having a low resolution). Consequently, we have also studied the effect of the quantization in 214GBd QPSK transmission. The resolution of the ADC in full bandwidth detection was 2 bits, and 5 bits ADC was considered in the case of the signal captured by the optical channelizer.

While InP-based oscilloscopes with ENOB of 5 bits at 110 GHz are available [79], as mentioned before, they are not suitable for real communication systems. Recently, 97GS/s ADC with 40 GHz analog front end bandwidth in 7nm FinFET was reported [80]. To achieve higher

sampling rates in CMOS digital signal processor ASICs and bridge the gap between high-speed optical inputs and bandwidth limited digitizers, utilization of a SiGe front-end was proposed [81]. By using a 1-to-4 analog demultiplexer in SiGe front end and time interleaving of four low-speed ADCs, the detection of up to 128 GBd symbol rates was enabled. In this configuration, the estimated resolution of the four output signals of the analog demultiplexer was more than 3-bit ENOB across the 6-dB bandwidth. Besides that, the 13 dB SNR of the received 128-Gbaud NRZ/OOK and PAM-4 signals corresponded to 2-bit ENOB [81]. Considering these reported effective number of bits for high-speed ADCs and the fact that ENOB is a monotonically decreasing function of bandwidth, it was reasonable to consider 2-bit ENOB ADC in full-bandwidth detection of 214 GBd QPSK signals.

As expected, the inexorable coarse quantization (with 2 bits) in the full bandwidth approach severely limits one's ability to maintain the signal integrity through digital signal processing and the QF (shown in Figure 4. 13) exhibits a significant drop. In sharp contrast, the higher resolution, ADCs associated with the optical channelizer (5 bits), results in as much as 6dB QF improvement in CD mitigation after the first span of 75km.

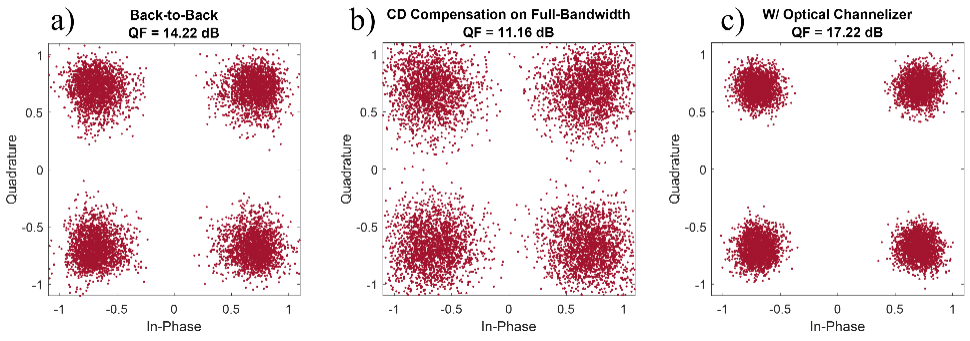

Figure 4. 13 Constellation of 214GBd QSK with 2 bits and 5 bits ADC in full-bandwidth and channelizers receivers, respectively: a) Back-to-Back. After transmission (L = 75 km) and CD compensation b) on Full-Bandwidth c) using Optical Channelizer.

For a broader insight, the QF versus transmission length for 214GBd QPSK in Figure 4. 14 shows that the higher resolution ADC in the optical channelizer significantly extends the transmission reach. The maximum transmission length in full bandwidth detection with 2bits ADC is only about 200km. In sharp contrast, the reach is more than tripled to 675km in CD compensation when relying on the optical channelizer.

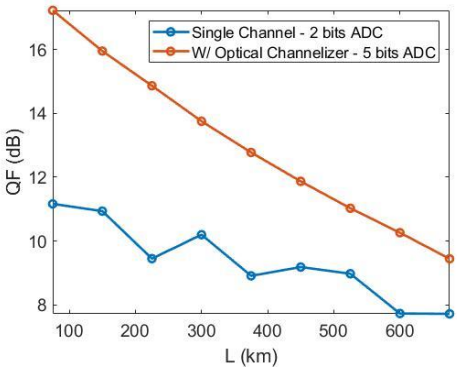

Figure 4. 14 QF versus transmission length in 214GBd QPSK transmission with 2 bits ADC in full-bandwidth, and 5 bits ADC in optical channelizer receivers (In optical channelizer signal and LO laser linewidth is 102kHz and the pump laser linewidth is 25.5kHz).

4.4.Summary

In this chapter, we have presented rigorous simulation results on chromatic dispersion compensation in high baud rate signals employing 8 and 4-channel parametric optical channelizers in a single polarization. The simulated parametric channelizer covered 5.4 THz and was fully based on the extensive experiments previously conducted. The filter bank resulting from the parametric channelization had a channel spacing of 29.47 GHz. The results demonstrate that the very high-speed systems can benefit tremendously from higher resolution ADCs as compared to the full-bandwidth approach, for high baud rate signals since it allows preservation of the signal integrity after propagation and successful CD compensation in transmission lengths up to 600km and 400km in 214GBd QPSK and 107GBd 16-QAM, respectively. In particular, higher resolution

ADC allowed by the parametric channelizer processor results in 6dB QF improvement even at the transmission over only 75km. More importantly, the transmission reach (assuming the FEC threshold of 10 dB Q factor, for a simple block code) enabled by the channelization corresponded to more than 675 km, as compared to only 200 km reach in the standard full-bandwidth approach limited by the corresponding 2bits ADC resolution. The demonstrated reach tripling not only speaks to the benefits of the channelization approach but also fully justifies the added complexity of the parametric channelization.

All things considered, the proposed physically assisted CD mitigation based on a parametric optical channelizer has been shown to be highly beneficial for channel impairment mitigation and extending the transmission reach in high-speed optical transmission. The method serves as an effective bridge between the high bandwidth offered by fiber-optic medium and high-quality low-speed electronic components– in particular the high-resolution digitizers, as well as the pipelined low-speed digital signal processing. Significant additional performance improvements of the physically assisted detection are readily possible by further optimization of the parametric channelizer performance.

Chapter 4, in part, is a reprint of the material submitted to IEEE Photonics Journal, titled "Parametric Channelizer Assisted Chromatic Dispersion Compensation in High-Baud Rate Coherent Systems" by Zahra Serahati, Nikola Alic, and Stojan Radic. The dissertation author was the primary investigator and the primary author of this article..

Chapter 5 Conclusion

5.1.Dissertation Summary

As has been pointed out, as well, made abundantly clear by the presented results in this thesis, high-capacity communication systems are needed to meet the demand of the extensive growing trend of data traffic. The aim of the new generation 5G mobile network is to serve as a unified platform for various users and applications, including person-to-person, M2M, and person-to-machine connection, and, as such, it covers a wide range of frequencies with different signal bandwidths and carrier spacing. The data traffic growth also requires an immense capacity expansion in coherent optical fiber transmission systems. This clearly points out an extensive need for high-speed optical and electrical components in the backbone of our communication networks. In addition, as has also been shown in this thesis, high-resolution and high-speed ADCs are required in these systems. Thus, we face the fundamental limit of ADCs' resolution at high speeds (i.e wide bandwidths). Also, simultaneous programmability and rapid frequency-tunability in RF subsystems appear to be critical features in the new network. Considering these challenges in the wireless and optical communication systems and potentials of the photonic technologies, in this dissertation, we proposed and investigated the utilization of hybrid optoelectronic subsystems in high-speed and high-capacity communication networks, instead of their all-electronic counterparts. Using electronic and photonic components with bandwidths compatible with the commercially available devices, these hybrid subsystems offer functionalities with equivalent or even better performance, unprecedented in the all-electronic subsystems.

In chapter 2, we reviewed the background regarding the material discussed in this dissertation. First, pulse propagation through fiber and its governing equations were discussed. Then, the chromatic dispersion effect in the optical fibers, which played somewhat contradicting roles in this dissertation was explained. The chromatic dispersion effect was taken advantage of to introduce a frequency-dependent delay and in turn, allow for narrow RF filter construction. In contrast, CD as the major impairment in fiber optic systems has been digitally mitigated to retrieve the data that had been disintegrated by propagation through the fiber. Then, coherent modulation, detection, and metrics for quantifying the optical signal quality were discussed. The configuration of a digital coherent optical transmission system was briefly reviewed, following the signal from the transmitter to the receiver. The digital signal processing chain in the coherent transmitter and receiver was discussed. Particularly, the chromatic dispersion detriment in coherent optical transmission systems, causing vast intersymbol interference, as well as mitigation of this effect using digital signal process (or digital filters) were explained.

In chapter 3, the demonstration and characterization of a new- first of its kind - sub-GHz flat-top comb-based FIR RF-photonic filter was presented. The flat-top spectral shape, for filtering the Nyquist-shaped RF signals in communication channels, and the less than GHz bandwidth in practical RF filters are among their critical features. However, the previously reported comb-based RF-photonic filters rarely had flat-top spectral shape, or the bandwidth of those flat-top filters exceeded 1.5 GHz. By phase and amplitude control of a wideband 25GHz-pitched parametric optical frequency comb, we have realized a narrowband flat-top comb-based RF-photonic filter. The high number of comb lines used in our implementation enabled the realization of a sub-GHz filter. However, the utilization of a wide bandwidth parametric optical frequency comb, 45nm

window, revealed the detrimental effect of higher-order dispersion of the optical fiber on the RF-photonic filter shape. The notable compliance of the implemented RF-photonic filter to the designed filter and its shape-invariant center frequency tuning was enabled by a precise higher-order dispersion compensation employing a pulse shaper. The up to fourth-order dispersion compensation, which was implemented for the first time in these filters, enabled the characterization of a 75 MHz-wide high-quality flat-top filter.

In chapter 3, first, the theory and working principle of the comb-based RF-photonic filter as well as the equations for phase correction using pulse shaper and up to fourth-order dispersion compensation were presented. Then, the implemented experimental setup was explained. First, the filter transfer function was characterized by a VNA. By varying the optical delay in one arm of the interferometer in the setup, the filter center frequency was tuned from 10.74 to 14.16 GHz. Precise control of the higher-order dispersion of fiber resulted in keeping the filter bandwidth and spectral shape almost the same in this frequency tuning. The integrity of the filter was further verified by retrieval of a set of digitally modulated RF channels. The single-channel RF signals with 400 to 900 MBaud symbol rates for QPSK and 16-QAM modulation format were successfully recovered at three different center frequencies. Additionally, successful retrieval of seven 100 MBaud subchannels with 104 MHz spacing carrying QPSK and 16-QAM modulation was also demonstrated. The shape-invariant filter center frequency tuning and robust retrieval of almost 5G-compatible RF channels promise their application in the 5G network which covers a wide range of frequencies and different signal bandwidths. Besides simultaneous programmability and rapid frequency tuning capabilities in these filters, another outstanding advantage of them is to relax the high-resolution ADC requirement.

In chapter 4, we have proposed and investigated the parametric channelizer-assisted chromatic dispersion compensation in high baud rate coherent systems. Chromatic dispersion penalty which scales with the signal square of the (symbol) signal rate limits the transmission reach if not compensated precisely. Consequently, as the number of capacity and bandwidth-hungry services keeps increasing and, accordingly, the baud rate of single-carrier QAM optical coherent signals, the need for reliable and cost-effective approaches to detect and digitally process the high-speed coherent signals continues to be of prime importance. In chapter 4, first, the principle of parametric optical channelizer, sub-band chromatic dispersion compensation, and signal reconstruction using a digital filter bank was explained. Then, the details of our parametrical optical channelizer design were provided. The numerical simulation was performed in VPIphotonics software. It was demonstrated that channelizer-assisted CD compensation, without considering the analog-to-digital conversion in the receiver, supports 214GBd QPSK and 107GBd 16-QAM optical signal transmission up to 600km and 400km, respectively. The channelizer-assisted chromatic dispersion compensation manifested its exceptional benefit when analog-to-digital conversion and ADC resolution reduction at higher bandwidths.was taken into account. Specifically, a 5bit-ADC consistent with the narrow bandwidth processing enable with the parametric channelizer, a 6dB QF improvement over the full-bandwidth detection with 2bits ADC, was shown in CD compensation of 214GBd QPSK optical signal (after 75km transmission length). More importantly, considering higher-resolution digitization in the optical channelizer, the maximum transmission reach was extended from 200km in full-bandwidth to 675km in channelizer-assisted CD compensation.

5.2.Future Outlook

5.2.1. Flat-top Comb-based RF-photonic Filter

In the implementation of the flat-top comb-based RF-photonic filter, presented in chapter 3, our main goal was to achieve a narrowband flat-top spectral shape which supports the Nyquist-shaped RF signals. And the sub-GHz filter bandwidth, which was achieved for the first time in this type of filters, make these filters finally to be more of practical use. We have successfully achieved this goal by using a wideband parametric comb with 221 comb lines, the highest number of the comb lines or filter taps reported so far in these filters. Moreover, we have managed to precisely mitigate up to fourth-order dispersion of the fiber, which was also proposed and implemented for the first time, to achieve the designed flat-top filter shape.

It should be noted that RF gain and Noise Figure are the two critical parameters defining the radio frequency performance of the RF systems [82], [83]. The measurement of these parameters was not in the scope of this thesis. In our configuration, we have used a single square-law photodetector to detect the filtered RF signal. However, using balanced detection, instead, will result in a 6dB RF gain increase and common noise cancelation [83]. Therefore, a worthwhile approach to continue this research is to implement balance detection in our flat-top filter configuration and measure the RF gain and NF.

5.2.2. Channelizer assisted chromatic dispersion compensation in high baud rate coherent systems

In the other area of our investigation – that of channelizer assisted CD compensation, discussed in chapter 4, we have considered the effect of digitization in the receiver. And owing to the channelizer-assisted detection, no high-speed electro-optic (EO) or optoelectronic (OE)

devices needed to be used. However, in the generation of the high baud rate QAM optical signals, we have not considered any non-ideality. Different schemes for the generation of high baud-rate optical signals using the available limited bandwidth EO/OE devices have been proposed, including electronic time-division multiplexing (ETDM), high-speed DACs, multiple spectral slices synthesis multiplexing, and digital bandwidth interleaving (DBI) [3], [58]. As a next step, it would be beneficial to consider the generation of the high baud rate optical signal with available limited bandwidth EO/OE devices using one of the approaches reported so far. It is foreseeable that these limitations would affect the quality of the generated high baud-rate optical signal and consequently the maximum transmission reach.

As mentioned before, CD compensation is one of the most power-hungry blocks of the DSP chain in coherent systems. Different approaches for digital CD mitigation have been proposed and implemented previously, including the time-domain digital filter [30], [84], overlap frequency domain equalizer [29], or CD compensation in digital filter banks [85]. The computational complexity of these methods has also been studied [86], [87]. For the digital CD compensation in each sub-channel of our optical channelizer, each of these algorithms, their computational complexity and performance ought to be studied. This investigation would certainly help to decide the best approach and the algorithm for a given signal baud rate and transmission length and clarify the possible trade-offs between the computational complexity and the quality of the recovered signal.

Lastly, after detailed and robust numerical simulations of the system, one can move to experimental implementation of the system and troubleshoot any possible challenges in the implementation of the physical system.

Bibliography

[1] F. Pittalà, M. Schaedler, G. Khanna, S. Calabrò, and M. Kuschnerov, "220 GBaud Signal Generation Enabled by a Two-channel 256 GSa / s Arbitrary Waveform Generator and Advanced DSP," no. 1, pp. 2–5, 2020.

[2] J. Zhang, J. Yu, and H. C. Chien, "WDM Transmission of 16-Channel Single-Carrier 128-GBaud PDM-16QAM signals with 6.06 b/s/Hz SE," Opt. Fiber Commun. Conf., 2017.

[3] S.A. Li, H. Huang, Z. Pan, R. Yin, Y. Wang, Y. Fang, Y. Zhang, C. Bao, Y. Ren, Z. Li, and Y. Yue, "Enabling Technology in High-Baud-Rate Coherent Optical Communication Systems," IEEE Access, vol. 8, pp. 111318–111329, 2020.

[4] Cisco, "Cisco Annual Internet Report (2018–2023) White Paper," 2020. [Online]. Available: https://www.cisco.com/c/en/us/solutions/collateral/executive-perspectives/annual-internet-report/white-paper-c11-741490.html.

[5] Qualcomm, "What's in the future of 5G?" [Online]. Available: https://www.qualcomm.com/documents/whats-future-5g-millimeter-wave.

[6] L. Marijanović and S. Member, "Multiplexing Services in 5G and Beyond : Optimal Resource Allocation Based on Mixed Numerology and Mini-Slots," vol. 8, pp. 209537–209555, 2020.

[7] J. L. Carcel, B. Mouhouche, M. Fuentes, E. Garro, and D. Gomez-Barquero, "IMT-2020 Key Performance Indicators: Evaluation and Extension Towards 5G New Radio Point-to-Multipoint," IEEE Int. Symp. Broadband Multimed. Syst. Broadcast. BMSB, vol. 2019-June, no. June 2019, 2019.

[8] Ali A. Zaidi, Robert Baldemair, Hugo Tullberg, Hakan Bjorkegren, Lars Sundstrom, Jonas Medbo, Caner Kilinc, and Icaro Da Silva., "Waveform and Numerology to Support 5G Services and Requirements," IEEE Commun. Mag., vol. 54, no. 11, pp. 90–98, 2016.

[9] RohdeSchwarz, "5G Overview-Mobile Technologies and the Way to 5G," 2017. [Online]. Available: https://cdn.rohde-schwarz.com/it/seminario/hi_technology_forum/Sibila_5G_Mobile_Technologies_and_the_way_to_5G.pdf.

[10] C. Schmidt, C. Kottke, V. Jungnickel, and R. Freund, “High-speed digital-to-analog converter concepts,” Next-Generation Opt. Commun. Components, Sub-Systems, Syst. VI, vol. 10130, no. June 2018, p. 101300N, 2017.

[11] T. Drenski and J. C. Rasmussen, “ADC / DAC and ASIC technology trends,” vol. 1, no. 1, pp. 2019–2021, 2019.

[12] F. Buchali, K. Schuh, S. T. Le, X. Q. Du, M. Grözing, and M. Berroth, “A SiGe HBT BiCMOS 1-to-4 ADC frontend supporting 100 GBaud PAM4 reception at 14 GHz digitizer bandwidth,” Opt. InfoBase Conf. Pap., vol. Part F160-, pp. 2019–2021, 2019.

[13] D. Novak and J. Capmany, “Microwave photonics combines two worlds,” Nat. Photonics, vol. 1, no. 6, pp. 319–319, 2007.

[14] A. E. Willner, S. Khaleghi, M. R. Chitgarha, and O. F. Yilmaz, “All-Optical Signal Processing,” J. Light. Technol., vol. 32, no. 4, pp. 660–680, 2014.

[15] S. Wabnitz and B. Eggleton, All-Optical Signal Processing, Data Communication and Storage Applications. 2015.

[16] E. Myslivets, B. P. P. Kuo, N. Alic, and S. Radic, “Generation of wideband frequency combs by continuous-wave seeding of multistage mixers with synthesized dispersion,” Opt. Express, vol. 20, no. 3, p. 3331, 2012.

[17] V. Ataie, E. Myslivets, B. P. P. Kuo, N. Alic, and S. Radic, “Spectrally equalized frequency comb generation in multistage parametric mixer with nonlinear pulse shaping,” J. Light. Technol., vol. 32, no. 4, pp. 840–846, 2014.

[18] Z. Tong, A. O. J. Wiberg, E. Myslivets, B. P. P. Kuo, N. Alic, and S. Radic, “Spectral linewidth preservation in parametric frequency combs seeded by dual pumps,” Opt. Express, vol. 20, no. 16, p. 17610, 2012.

[19] G. G. P. Agrawal, P. L. Kelley, I. P. Kaminow, and G. G. P. Agrawal, “Nonlinear fiber optics,” Nonlinear Sci. Daw. 21st Century, no. Springer, Berlin, Heidelberg, 2001.

[20] David Keun Cheng, Field and wave electromagnetics. Pearson Education India, 1989.

[21] G. C. Papen and R. E. Blahut, Lightwave Communications. Cambridge University Press, 2019.

[22] K. Kikuchi, "Fundamentals of Coherent Optical Fiber Communications," J. Light. Technol., vol. 34, no. 1, pp. 157–179, 2016.

[23] I. P. Kaminow, T. Li, and A. E. Willner, Optical Fiber Telecommunications Components and Subsystems, Sixth Edit., vol. VIA. Elsevier, 2013.

[24] W. Freude, R. Schmogrow, B. Nebendahl, M. Winter, A. Josten, D. Hillerkuss, S. Koenig, J. Meyer, M. Dreschmann, M. Huebner, and C. Koos, "Quality metrics for optical signals: Eye diagram, Q-factor, OSNR, EVM and BER," Int. Conf. Transparent Opt. Networks, vol. 1, pp. 3–6, 2012.

[25] Govind P. Agrawal, Fiber-optic communication systems. John Wiley & Sons, 2012.

[26] M. S. Faruk and S. J. Savory, "Digital Signal Processing for Coherent Transceivers Employing Multilevel Formats," J. Light. Technol., vol. 35, no. 5, pp. 1125–1141, 2017.

[27] D. S. Ly-Gagnon, S. Tsukamoto, K. Katoh, and K. Kikuchi, "Coherent detection of optical quadrature phase-shift keying signals with carrier phase estimation," J. Light. Technol., vol. 24, no. 1, pp. 12–20, 2006.

[28] K. V. Cartwright and E. J. Kaminsky, "Blind phase recovery in cross QAM communication systems with the Reduced-Constellation Eighth-Order Estimator," GLOBECOM - IEEE Glob. Telecommun. Conf., vol. 1, no. 12, pp. 388–392, 2005.

[29] R. Kudo, T. Kobayashi, K. Ishihara, Y. Takatori, A. Sano, and Y. Miyamoto, "Coherent Optical Single Carrier Transmission Using Overlap Frequency Domain Equalization for Long-Haul Optical Systems," J. Light. Technol., vol. 27, no. 16, pp. 3721–3728, 2009.

[30] S. J. Savory, “Digital filters for coherent optical receivers,” Opt. Express, vol. 16, no. 2, p. 804, 2008.

[31] J. Capmany and D. Novak, “Microwave photonics combines two worlds,” Nat. Photonics, vol. 1, no. 6, pp. 319–330, 2007.

[32] D. Marpaung, J. Yao, and J. Capmany, “Integrated microwave photonics,” Nat. Photonics, vol. 13, no. 2, pp. 80–90, 2019.

[33] H. J. Kim, D. E. Leaird, and A. M. Weiner, “Rapidly Tunable Dual-Comb RF Photonic Filter for Ultrabroadband RF Spread Spectrum Applications,” IEEE Trans. Microw. Theory Tech., vol. 64, no. 10, pp. 3351–3362, 2016.

[34] J. Lee, E. Tejedor, K. Ranta-aho, H. Wang, K.T. Lee, E. Semaan, E. Mohyeldin, J. Song, C. Bergljung and S. Jung, “Spectrum for 5G: Global Status, Challenges, and Enabling Technologies,” IEEE Commun. Mag., vol. 56, no. 3, pp. 12–18, 2018.

[35] J. Capmany, B. Ortega, D. Pastor, and S. Sales, “Discrete-time optical processing of microwave signals,” J. Light. Technol., vol. 23, no. 2, pp. 702–723, 2005.

[36] A. M. Weiner, “Femtosecond pulse shaping using spatial light modulators,” Rev. Sci. Instrum., vol. 71, no. 5, pp. 1929–1960, 2000.

[37] J. Yao, “A Tutorial on Microwave Photonics,” Photonics Soc. Newsl., vol. 24, no. April, pp. 4–12, 2012.

[38] A. Ortigosa-Blanch, J. Mora, J. Capmany, B. Ortega, and D. Pastor, “Tunable radio-frequency photonic filter based on an actively mode-locked fiber laser,” Opt. Lett., vol. 31, no. 6, p. 709, 2006.

[39] X. Xue, X. Zheng, H. Zhang, and B. Zhou, “Spectrum-sliced microwave photonic filter with an improved dynamic range based on a LiNbO 3 phase modulator and balanced detection,” IEEE Photonics Technol. Lett., vol. 24, no. 9, pp. 775–777, 2012.

[40] X. Xue, X. Zheng, H. Zhang, and B. Zhou, “Widely tunable single-bandpass microwave

photonic filter employing a non-sliced broadband optical source," Opt. Express, vol. 19, no. 19, p. 18423, 2011.

[41] E. Hamidi, D. E. Leaird, and A. M. Weiner, "Tunable Programmable Microwave Photonic Filters Based on an Optical Frequency Comb," IEEE Trans. Microw. Theory Tech., vol. 58, no. 11, pp. 3269–3278, 2010.

[42] M. Song, V. Torres-Company, and A. M. Weiner, "Comparative Study of Noise Performance of Microwave Photonic Filters Based on Coherent and Incoherent Multi-wavelength Light Sources," IEEE Int. Top. Meet. Microw. Photonics, vol. 24, no. 14, pp. 331–334, 2012.

[43] Y. M. Chang, H. Chung, and J. H. Lee, "High Q Microwave Filter Using Incoherent , Continuous-Wave Supercontinuum and Dipsersion-Profiled Fiber," IEEE Photonics Technol. Lett., vol. 19, no. 24, pp. 2042–2044, 2007.

[44] X. Xue, X. Zheng, H. Zhang, and B. Zhou, "Analysis and compensation of third-order dispersion induced RF distortions in highly reconfigurable microwave photonic filters," J. Light. Technol., vol. 31, no. 13, pp. 2263–2270, 2013.

[45] G. Peraita, A. J. Torregrosa, H. Maestre, and C. R. Fernandez-Pousa, "Broadband linearization of dispersive delay line using a chirped fiber bragg grating," IEEE Photonics Technol. Lett., vol. 27, no. 10, pp. 1044–1047, 2015.

[46] X. Yi, T. X. H. Huang, L. Li, and R. A. Minasian, "Overcoming tap-delay-variation induced distortion in microwave photonic filters," IEEE Photonics Technol. Lett., vol. 24, no. 8, pp. 691–693, 2012.

[47] D. Zou, X. Zheng, and S. Li, "High-Q microwave photonic filter with self-phase modulation spectrum broadening and third-order dispersion compensation," CHINESE Opt. Lett., vol. 12, no. 8, pp. 10–13, 2014.

[48] M. Song, V. Torres-Company, R. Wu, A. J. Metcalf, and A. M. Weiner, "Compression of ultra-long microwave pulses using programmable microwave photonic phase filtering with > 100 complex-coefficient taps," Opt. Express, vol. 22, no. 6, p. 6329, 2014.

[49] H. J. Kim, A. Rashidinejad, and A. M. Weiner, “Low-Loss Ultrawideband Programmable RF Photonic Phase Filter for Spread Spectrum Pulse Compression,” IEEE Trans. Microw. Theory Tech., vol. 63, no. 12, pp. 4178–4187, 2015.

[50] M. Song, C. M. Long, R. Wu, D. Seo, D. E. Leaird, and A. M. Weiner, “Reconfigurable and tunable flat-top microwave photonic filters utilizing optical frequency combs,” IEEE Photonics Technol. Lett., vol. 23, no. 21, pp. 1618–1620, 2011.

[51] X. Xue, Y. Xuan, H.J. Kim, J. Wang, D.E. Leaird, M. Qi, and A.M. Weiner, “Programmable single-bandpass photonic rf filter based on kerr comb from a microring,” J. Light. Technol., vol. 32, no. 20, pp. 3557–3565, 2014.

[52] B. Razavi, RF Microelectronics, Vol 2. New Jersey: Prentice Hall, 1998.

[53] Amitabha Ghosh, “5G New Radio (NR) : Physical Layer Overview and Performance,” IEEE Commun. Theory Work., 2018.

[54] E. Hamid, R. Wu, V. R. Supradeepa, C. M. Long, D. E. Leaird, and A. M. Weiner, “Tunable radio frequency photonic filter based on intensity modulation of optical combs,” 2010 IEEE Int. Top. Meet. Microw. Photonics, pp. 393–396, 2010.

[55] H. Hu, V. Ataie, E. Myslivets, and S. Radic, “Optical Comb Assisted OFDM RF Receiver,” J. Light. Technol., 2019.

[56] S. A. Tretter, Communication System Design Using DSP Algorithms. Springer Science & Business Media, 2008.

[57] F. Buchali, “Beyond 1 Tbit / s transmission using high- speed DACs and analog multiplexing,” pp. 1–28, 2021.

[58] F. Hamaoka, “Ultra-Wideband Transmission and High-Symbol Rate Signal Handling Technologies,” 2020 Opt. Fiber Commun. Conf. Exhib. OFC 2020 - Proc., 2020.

[59] J. Yu and N. Chi, Digital Signal Processing In High-Speed Optical Fiber Communication Principle and Application. 2020.

[60] P. J. Winzer, D. T. Neilson, and A. R. Chraplyvy, “Fiber-optic transmission and networking: the previous 20 and the next 20 years [Invited],” Opt. Express, vol. 26, no. 18, p. 24190, 2018.

[61] Hank Zumbahlen, Linear circuit design handbook. Newnes, 2011.

[62] M. Malekiha, I. Tselniker, and D. V. Plant, “Chromatic dispersion mitigation in long-haul fiber-optic communication networks by sub-band partitioning,” Opt. Express, vol. 23, no. 25, p. 32654, 2015.

[63] M. Kuschnerov, T. Bex, and P. Kainzmaier, “Energy efficient digital signal processing,” Opt. Fiber Commun. Conf. OFC 2014, pp. 14–16, 2014.

[64] B. S. G. Pillai, B. Sedighi, K. Guan, N.P. Anthapadmanabhan, W. Shieh, K.J. Hinton,. and R.S. Tucker, “End-to-end energy modeling and analysis of long-haul coherent transmission systems,” J. Light. Technol., vol. 32, no. 18, pp. 3093–3111, 2014.

[65] J. M. Estarán, S. Almonacil, R. Rios-Müller, H. Mardoyan, P. Jenneve, K. Benyahya, C. Simonneau, S. Bigo, J. Renaudier, and G. Charlet, “Sub-Baudrate Sampling at DAC and ADC : Toward 200G per Lane IM/DD Systems,” J. Light. Technol., vol. 37, no. 6, pp. 1536–1542, 2019.

[66] B. Murmann, “ADC Performance Survey 1997–2017 (ISSCC and VLSI Symposium),” 2017.

[67] F. Buchali, X. Q. Du, K. Schuh, S. T. Le, M. Grozing, and M. Berroth, “A SiGe HBT BiCMOS 1-to-4 ADC Frontend Enabling Low Bandwidth Digitization of 100 GBaud PAM4 Data,” J. Light. Technol., vol. 38, no. 1, pp. 150–158, 2020.

[68] A. Zandieh, N. Weiss, T. Nguyen, D. Haranne, and S. P. Voinigescu, “128-GS/s ADC Front-End with over 60-GHz Input Bandwidth in 22-nm Si/SiGe FDSOI CMOS,” in 2018 IEEE BiCMOS and Compound Semiconductor Integrated Circuits and Technology Symposium, BCICTS 2018, 2018, pp. 271–274.

[69] F. Hamaoka, M. Nakamura, M. Nagatani, H. Wakita, and T. Kobayashi, “Ultra-wideband Optical Receiver Using Electrical Spectrum Decomposition Technique,” no. 1, pp. 2–5, 2020.

[70] N. K. Fontaine, G. Raybon, B. Guan, A. Adamiecki, P.J. Winzer, R. Ryf, A. Konczykowska, F. Jorge, J.Y. Dupuy, L.L Buhl, and S. Chandrashekhar, “228-GHz coherent receiver using digital optical bandwidth interleaving and reception of 214-GBd (856-Gb/s) PDM-QPSK,” Eur. Conf. Exhib. Opt. Commun. ECEOC 2012, pp. 3–5, 2012.

[71] X. Xie, Y. Dai, K. Xu, J. Niu, R. Wang, L. Yan, and J. Lin, “Broadband photonic RF channelization based on coherent optical frequency combs and I/Q demodulators,” IEEE Photonics J., vol. 4, no. 4, pp. 1196–1202, 2012.

[72] A. O. J. Wiberg, D.J. Esman, L. Liu, J.R. Adleman, S. Zlatanovic, V. Ataie, E. Myslivets, B.P.P. Kuo, N. Alic, E.W. Jacobs, and S. Radic, “Coherent filterless wideband microwave/millimeter-wave channelizer based on broadband parametric mixers,” J. Light. Technol., vol. 32, no. 20, pp. 3609–3617, 2014.

[73] B. P. P. Kuo, E. Myslivets, N. Alic, and S. Radic, “Wavelength multicasting via frequency comb generation in a bandwidth-enhanced fiber optical parametric mixer,” *J. Light. Technol.*, vol. 29, no. 23, pp. 3515–3522, 2011.

[74] C. J. McKinstrie, S. Radic, and A. R. Chraplyvy, “Parametric amplifiers driven by two pump waves,” *IEEE J. Sel. Top. Quantum Electron.*, vol. 8, no. 3, pp. 538–547, 2002.

[75] Z. Serahati, E. Temprana, E. Myslivets, V. Ataie, N. Alic, and S. Radic, “Demonstration of a Sub-GHz Flat-Top Comb-Based RF-Photonic Filter Enabled by Fourth-Order Dispersion Compensation,” *J. Light. Technol.*, vol. 38, no. 6, pp. 1194–1201, 2020.

[76] A. V. Oppenheim, A. S. Willsky, and S. H. Nawab, *Signals and systems*. prentice-hall signal processing series, 1996.

[77] M. Vetterli and D. Le Gall, “Perfect Reconstruction FIR Filter Banks: Some Properties and Factorizations,” *IEEE Trans. Acoust.*, vol. 37, no. 7, pp. 1057–1071, 1989.

[78] “International Telecommunication Union Telecommunication Standardization Sector

(ITU-T), Series G: Transmission Systems and Media," 2004.

[79] Keysight, "Infiniium UXR-series oscilloscope," 2019. [Online]. Available: https://www.keysight.com/us/en/assets/7018-06242/data-sheets/5992-3132.pdf.

[80] R. L. Nguyen, A.M. Castrillon, A. Fan, A. Mellati, B.T. Reyes, C. Abidin, E. Olsen, F. Ahmad, G. Hatcher, J. Chana, and L. Biolato, "A Highly Reconfigurable 40-97GS/s DAC and ADC with 40GHz AFE Bandwidth and Sub-35fJ/conv-step for 400Gb/s Coherent Optical Applications in 7nm FinFET," *2021 IEEE Int. Solid- State Circuits Conf.*, pp. 136–138, 2021.

[81] P. Thomas, T. Tannert, M. Grözing, M. Berroth, Q. Hu, and F. Buchali, "1-to-4 Analog Demultiplexer With up to 128 GS / s for Interleaving of Bandwidth-Limited Digitizers in Wireline and Optical Receivers," *IEEE J. Solid-State Circuits*, pp. 1–13, 2021.

[82] H. J. Kim, D. E. Leaird, and A. M. Weiner, "Improved RF performance of a comb-based microwave photonic filter using a balanced photodetector," *2013 IEEE Int. Top. Meet. Microw. Photonics, MWP 2013*, pp. 80–83, 2013.

[83] H. J. Kim, D. E. Leaird, A. J. Metcalf, and A. M. Weiner, "Comb-Based RF photonic filters based on interferometric configuration and balanced detection," *J. Light. Technol.*, vol. 32, no. 20, pp. 3478–3488, 2014.

[84] A. Eghbali, H. Johansson, O. Gustafsson, and S. J. Savory, "Optimal least-squares FIR digital filters for compensation of chromatic dispersion in digital coherent optical receivers," *J. Light. Technol.*, vol. 32, no. 8, pp. 1449–1456, 2014.

[85] K. P. Ho, "Subband equaliser for chromatic dispersion of optical fibre," *Electron. Lett.*, vol. 45, no. 24, pp. 1224–1226, 2009.

[86] J. Leibrich and W. Rosenkranz, "Frequency domain equalization with minimum complexity in coherent optical transmission systems," *Opt. InfoBase Conf. Pap.*, pp. 1–3, 2010.

[87] T. Xu, G. Jacobsen, S. Popov, M. Forzati, J. Mårtensson, M. Mussolin, J. Li, K. Wang, Y. Zhang, and A.T. Friberg , "Frequency-domain chromatic dispersion equalization using overlap-add methods in coherent optical system," *J. Opt. Commun.*, vol. 32, no. 2, pp. 131–135, 2011.